PEOPLE'S DEMOCRATIC REPUBLIC OF ALGERIA MINISTRY OF HIGHER EDUCATION AND SCIENTIFIC RESEARCH

UNIVERSITY OF YAHYA FARES-MEDEA



FACULTY OF TECHNOLOGY

MASTER'S DEGREE DISSERTATION IN MATERIALS PROCESS ENGINEERING

EFFECT OF THE TERMINAL GROUPS Tx ON THE STRUCTURAL AND MECHANICAL PROPERTIES OF MXene CR_2C MATERIAL: CASE OF THE OH AND O GROUPS

- PREPARED BY:

  BOUAKKACHA IMANE

  CHEBANE HAYAT

- DIRECTED BY:

  PR. KREA MOHAMED

Batch of 2023/2024 Graduates

بِسْمِ ٱللَّهِ ٱلرَّحْمَٰنِ ٱلرَّحِيمِ

Acknowledgement:

(... وَآخِرُ دَعْوَاهُمْ أَنِ الْحَمْدُ لِلَّهِ رَبِّ الْعَالَمِينَ)

I would like to convey my profound appreciation to Mr Krea Mohamed for his invaluable guidance, unwavering support, his patience with us, and insightful feedback throughout the duration of this project. His expertise have been instrumental in shaping the direction and success of this endeavor.

I am also deeply thankful to my esteemed teachers for their guidance, and mentorship throughout my academic journey.

I would like also to express my sincere gratitude to the jury members for their valuable time and insightful feedback.

I am profoundly grateful to my beloved family for their unwavering love, their belief in me, constant encouragement, and understanding have been the pillars of strength that sustained me through challenges and triumphs alike. This achievement is as much theirs as it is mine, and I am forever grateful for their presence in my life.

I would like to extend my heartfelt appreciation to my dear friends. Their friendship has been a source of strength, laughter, and motivation, making even the most challenging moments feel manageable.

I am making this project not only for marks but to also increase my knowledge.

THANKS AGAIN TO ALL WHO HELPED ME EVEN THE FICTIONAL ONE, FOR ALWAYS BEING THERE FOR ME, CHEERING ME ON, AND INSPIRING ME TO REACH FOR THE STARS

DEDICATION:

(وَمَا تَوْفِيقِي إِلَّا بِاللَّهِ ۚ عَلَيْهِ تَوَكَّلْتُ وَإِلَيْهِ أُنِيبُ)

"الحمد لله حمد الشاكرين، والحمد لله في كل وقت وحين. الحمد لله حمداً على كل النعم. والحمد لله على حمد النعم .والحمد لله حمداً يليق برب النعم .فيا ربنا لك الحمد"

I shall then dedicate the result of my modest labor:

To my biggest blessings my mom MERAH. F, and dad BOUAKKACHA Mohamed, whose steadfast love and support have motivated me to pursue education. Your words of wisdom and encouragement have also been a source of great gifts.

To my dear brother ABDALHAMID, and my beloved sisters, SIHAM and AYA, this achievement is a testament to our bond and the strength we draw from one another.

To my dear friends DONYA, LILA, YORA and SAMAH, thanks to our friendships, this journey has been incredibly rewarding as well as manageable. This accomplishment pays homage to the innumerable memories we have together.

To all family and relatives from near to far.

To everyone who prayed for me at the back of the invisible, to everyone who supported and assisted me. I beseech Allah to bestow upon everyone the greatest blessings both here on this world and in the hereafter.

IMANE.

To express my thanks to all those who contributed in many ways to the success of this study.

To my dear parents MHAMMED, and F.RAHALI, thank you for giving me support to reach my dreams. Accomplishing this would hopefully make you proud of me as much as I am proud of having you as my parents.

To my uncle HAMZA RAHALI, thank you for all the things you have done for me. I know you will be proud of me in doing this accomplishment.

HAYAT

ملخص:

تتعمق هذه الدراسة في تأثير مجموعات الإنهاء OH و O على الخواص الميكانيكية والهيكلية لـ Cr_2C MXene. باستخدام عمليات المحاكاة الحسابية المتوقعة على النهج المبدئي للنظرية الوظيفية للكثافة (DFT) استنادًا إلى طريقة الإمكانات الزائفة والموجة المستوية(PP-PW) ، نستكشف كيف تؤثر هذه النهايات على الخصائص المرنة، مثل الصلابة التي يتم استنتاجها من خلال القيم العالية لمعامل Young، بالإضافة إلى الاستقرار الهيكلي بما في ذلك أطوال حواف الخلية (a, b, c) لـ Cr_2C MXene. توضح النتائج التي توصلنا إليها الدور الدقيق لمجموعات الإنهاء في إملاء الأداء والتطبيقات المحتملة لـ MXenes الجديدة في المجالات المختلفة.

- الكلمات المفتاحية: الهيدروكسيل، الأكسجين، Cr2C MXene، حسابات المبادئ الأولية، الخصائص المرنة والهيكلية ، معامل يونغ، نظرية الكثافة الوظيفيه.

Abstract:

This study delves into the impact of termination groups OH and O on the mechanical and structural properties of Cr_2C MXene. Using computational simulations based on the ab initio approach of the functional theory of density (DFT) founded on the pseudo-potential and plane-wave (PP-PW) method, we explore how these terminations influence the elastic properties, such as the rigidity which is deduced through the high values of the Young modulus, as well as the structural stability including the lengths of the cell edges (a, b, c) of Cr_2C MXene. Our finding elucidate the nuanced role of termination groups in dictating the performance and potential applications of a new MXenes in various domains.

- Key words: hydroxyl, oxygen, Cr_2C MXene, ab-initio, elastic and structural properties, Young modulus, DFT.

Résumé:

Cette étude approfondit l'impact des groupes de terminaison OH et O sur les propriétés mécaniques et structurelles du Cr_2C MXène. En utilisant des simulations informatiques basées par l'approche ab initio de la théorie fonctionnelle de la densité (DFT) avec la méthode du pseudo-potentiel et des ondes planes (PP-PW), nous explorons comment ces terminaisons influencent les propriétés élastiques, telles que la rigidité qui se déduit des valeurs élevées du module d'Young, ainsi que de la stabilité structurelle incluant les

longueurs des bords des cellules (a, b, c) du Cr_2C MXene. Nos découvertes élucident le rôle nuancé des groupes de terminaison dans la détermination des performances et des applications potentielles d'un nouveau MXenes dans divers domaines.

- Mots clés : hydroxyle, oxygène, Cr2C MXène, ab-initio, propriétés élastiques et structurales, module d'Young, DFT.

SUMMARY

I MAX AND MXENES PHASES 5
I.1 MAX PHASES: 5
I.1.1 History of the MAX Phases: 5
I.1.2 Overview and the chemical composition of MAX phases: 5
I.1.3 The chemistry and crystal Structure of MAX phases: 6
I.1.4 Synthesis of MAX phases: 8
I.1.5 MAX phases property: 11
I.1.6 Potential applications of MAX phases: 11
I.2 MXENES PHASES: 12
I.2.1 History of MXenes Phases: 12
I.2.2 Overview and the Chemical composition of MXenes phases: 12
I.2.3 Synthesis of MXenes phases: 13
I.2.4 Applications of MXenes: 16
I.2.5 Conclusion: 17
II STRUCTURAL AND MECHANICAL PROPERTIES OF MXENES 19
II.1 Introduction: 19
II.2 Structural properties: 19
II.2.1 Structure of MXene: 19
II.2.2 Crystal and atomic structure of MXenes: 21
II.2.3 Types of structures: 22
II.3 Mechanical properties: 23
II.3.1 Elastic properties: 24
II.4 Other properties: 28
II.4.1 Magnetic properties: 28
II.4.2 Optical properties: 29
II.4.3 Conclusion: 29
III MXENES SURFACE TERMINATION AND THEIR EFFECTS 31
III.1 Introduction: 31
III.2 Surface terminating groups of MXenes: 31
III.3 Stability and surface groups of MXenes: 33
III.4 Effects of surface modification on MXene properties: 34
III.4.1 Influence of terminations on mechanical properties: 34
III.5 Conclusion: 35

IV STUDY OF THE GEOMETRIC AND ELASTIC PROPERTIES OF Cr_2CO_2 AND $Cr_2C(OH)_2$ MXENES. 38

IV.1 Introduction: 38

IV.2 Description of the crystal structure of the MXene Cr_2CO_2 and $Cr_2C(OH)_2$ phase material: 39

IV.3 Geometric optimization of the structures: 43

IV.3.1 Computes elasticity tensors: 45

IV.4 Variation of structural properties: 47

IV.4.1 Behavior of network constants: 47

IV.4.2 Variations of elastic properties: 50

IV.4.3 Study of the variation of the elasticity tensors: 51

IV.4.4 Effect of pressure variation on the elastic properties of Cr_2CO_2 and $Cr_2C(OH)_2$: 54

IV.4.5 Study of the ductility of Cr_2CO_2 and $Cr_2C(OH)_2$ structures: 57

IV.4.6 Chen and Tian hardness: 59

IV.5 GENERAL CONCLUSION: 61

FIGURE LIST

Figure I-1: Periodic table displaying the elements that make up the MAX phases: **A**: group A-element (blue), **X**: C and/or N (black), and **M**: early transition metal (red) [6]. 6
Figure I-2: Crystal structure of the 211, 312, and 413 MAX phases [9]. 7
Figure I-3: High-angle annular dark field TEM image, acquired along the [11$\bar{2}$0] zone axis of Ti3SiC2, showing twinning and the resulting characteristic "zig-zag" stacking of MAX phases [10]. 7
Figure I-4: **(a)** Liquid-phase sintering; **(b)** Solid-state sintering [6]. 8
Figure I-5: Schematic diagram illustrating the hot pressing technique [12]. 9
Figure I-6: Characteristics of the MAX phase ceramics [15]. 11
Figure I-7: Periodic table displaying MXenes compounds. The components of MXenes are color-coded. The bottom section displays the schematics of four common MXenes structures [3]. 13
Figure I-8: M–X and M–A bonds schematic in a MAX phase, with M_2X layers positioned between layers of a single A atom. Green, red and black spheres represent **M**, **A** and **X**, in that order [19]. 13
Figure I-9: **(a)** Schematic diagram of the synthesis of MXene by HF etching. **(b)** The synthesis and structure diagram of Ti_3C_2Tx MXene [4]. 14
Figure I-10: Schematic diagram of the synthesis of Ti_3C_2Tx MXene by fluoride etching [4]. 15
Figure I-11: Schematic of the reaction setup used for molten salt etching in a tube furnace under argon flow to minimize the interference of oxygen during etching. FESEM images of **(A)** Parent Ti_3AlC_2 MAX phase, **(B)** $Ti_3C_2T_x$ before KOH wash (freeze-dried), **(C)** $Ti_3C_2T_x$ after KOH wash (freeze-dried) [2]. 16
Figure II-1: The Chemical versatility of all currently available MXenes systems, including conventional $M_{n+1}X_n$ (n=1, 2, 3), double-M solid solutions, out-of-plane ordered, in-plane ordered double-M, and divacancy ordered MXene systems [17]. 20
Figure II-2: The 1D, 2D, 3D, and 0D structures of MXenes. **(A)** Two-dimensional structure of MXene Nano-sheets. Top view of the geometric structures of **(B)** zigzag and **(C)** armchair Ti2C Nano-ribbons. Yellow and green balls indicate Ti and C atoms, respectively. **(D)** The 3D M-Ti_3C_2Tx film. **(E)** The nonoxidized MXene-Ti_3C_2Tx quantum dots (NMQDs-Ti_3C_2Tx) prepared by micro-explosion method [25]. 20
Figure II-3: Crystal structures of two-dimensional (2D) M2X MXenes. **(a)** The Ti_2C MXene model comprises a rhombus unit cell (dashed line) with hexagonal symmetry (top view). It consists of trilayer configurations where the C atomic layer is sandwiched between two Ti atomic layers (bottom panel). **(b)**, **(c)** MXene models with two different surface termination group configurations [26]. 21
Figure II-4: The 14 bravais-lattices in 3d [27]. 22
Figure II-5: Predictions on the mechanical 2D stiffness for terminated M_2XTx MXene for different surface terminations including O_2, F_2, $(OH)_2$, and Cl_2 [4]. 23
Figure II-6: (a): 2D stiffness and elastic modulus of Tin+1Xn (X = C, N) MXene, which illustrate the effect of increasing flake thickness (n) on MXenes' mechanical stiffness. **(b)**: Prediction of the elastic modulus of terminated MXenes, which illustrates the effect of increased monolayer thickness due the surface terminations on the stiffness trends in MXene. [29] 23

Figure II-7: Stress- strain relationship curve [30]. 24
Figure II-8: The elastic constants of c11 for M_2CT_2 MXenes [34]. 27
Figure III-1: Schematic illustration of the $M_{n+1}X_nTx$ MXene structures, where M is an early transition metal, X is carbon and/or nitrogen, and Tx represents surface terminations of the outer metal layers [40]. 31
Figure III-2: Possible models for M_2XT_2 systems [42]. 33
FigureIV-1: (a) crystal structure of Cr_2CO_2, **(b)** $Cr_2C(OH)_2$ established by geometric optimization. 40
Figure IV-2: Open the MATERIAL STUDIO program. 40
Figure IV-3: Choose the import icon, then open the geometric file respectively. 41
Figure IV-4: Open files in the program appear as follows. 41
Figure IV-5: show symmetry parameter. 42
Figure IV-6: **(a)**: show the symmetry group, **(b)**: Operators symmetry, **(c)**: and the symmetry of $Cr_2C(OH)_2$ MXene. 42
Figure IV-7: **(a)**: show the symmetry group, **(b)**: Operators symmetry, **(c)**: and the symmetry of Cr_2CO_2 MXene. 43
Figure IV-8: (a): Access calculations from the CASTEP model, **(b)**, **(c)**, **(d)** and **(e)** parameters modified before optimization. 44
Figure IV-9: start and currently undergoing optimization. 45
Figure IV-10: optimization completed. 45
Figure IV-11: **(a)**: choose CASTEP then calculation. **(b)**: select the optimized geometry, choose elastic constants then press RUN. 46
Figure IV-12: starting the calculations. 46
Figure IV-13: results obtained after calculation and analysis. 47
Figure IV-14: (a), **(b)**: variation of the constants "a=b" as a function of pressure, **(c)**: variation of the a/c ratio as a function of pressure, **(d)**: variation of volume as a function of pressure, for the three MXenes, **(e)**: high pressure of Cr_2CO_2 for different lattice parameters. 50
Figure IV-15: (a), (b), (c), (d), (e), (f), (g): variations of the 7 elasticity tensors as a function of pressure for the three MXenes, **(h):** high pressure of Cr_2CO_2 for the 7 elasticity tensors. 54
Figure IV-16: (a), (b), (c), (d): variations of the elastic properties as a function of pressure for the three MXenes, **(e), (f):** high pressure of Cr_2CO_2 for different elastic properties. 57
Figure IV-17: (a): representation of the G/β ratio for the three MXenes. 59
Figure IV-18: Chen and Tian hardness for both Cr_2CO_2 and $Cr_2C(OH)_2$ MXenes. 60

TABLE LIST

CHAPTER II

Table II-1: Classification of crystal families and systems. Centering type, Laue group, Hermann-Mauguin point-group symbols, and space-group numbers (SGN) [28]. 22

CHAPTER III

Table III-1: Comparison of the advantages and disadvantages of various synthesis strategies. 32

CHAPTER IV

Table IV-1: The lattice parameters of Cr_2CO_2 and $Cr_2C(OH)_2$ MXenes..... 39
Table IV-2: Evolution of the lattice parameters of the Cr_2CO_2 structure depending on the pressure. 47
Table IV-3: Evolution of the lattice parameters of the $Cr_2C(OH)_2$ structure depending on the pressure. 48
Table IV-4: The stress tensors for (Cr_2CO_2)..... 50
Table IV-5: stress tensor values (Cr_2CO_2). 51
Table IV-6: stress tensor values ($Cr_2C(OH)_2$). 52
Table IV-7: Elastic properties behavior during compression (Cr_2CO_2). 54
Table IV-8: Elastic properties behavior during compression ($Cr_2C(OH)_2$)..... 55
Table IV-9: values of the ductility ratio and Cauchy pressure. 58
Table IV-10: values of Pugh ratio, shear modulus, Chen and Tian hardness for both materials. 59

LIST OF ABBREVIATIONS

- CNTs Carbon Nanotubes
- CVD Chemical Vapor Deposition
- DFT Density Functional Theory
- DMSO Dimethylsulfoxide
- EDX Energy Dispersive X-ray Analysis
- EELS Electron Energy Loss Spectroscopy
- EMI Electromagnetic Interference
- ESDs Electro Static Discharge Sensitive
- FCC Face-Centred Cubic Unit Cell
- GGA Generalized Gradient Approximation
- HCP Hexagonal Close Packing
- HF Hydrofluoric Acid
- HIP Hot Isostatic Pressing
- HP Hot Pressing
- MW Microwave Sintering
- PAM Polyacrylamide
- PLS Pulsed Laser Deposition
- Rf Radio Frequency
- SHS Self-Propagating High-Temperature
- SEM Scanning Electron Microscopy
- SPS Spark Plasma Sintering
- TEM Transmission Electron Microscopy
- UHMWPE Ultra-High Molecular Weight Polyethylene
- XAS X-ray Absorption Spectroscopy
- XPS X-ray Photoelectron Spectroscopy
- 2D Two-Dimensional
- 3D Three-Dimensional

GENERAL INTRODUCTION

GENERAL INTRODUCTION

Over the last decade, 2D materials have garnered more interest throughout the past ten years. They have potential uses in transistors, Li-ion batteries, pseudo- and double layer capacitors...etc. 2D single layers have distinct optical, mechanical, electrical, and magnetic properties as well as larger specific surface areas as compared to bulk layered materials. These characteristic allow for the exploration of new 2D systems [1].

Since the discovery in 2004 of the special features of single-layer graphen, research on 2D materials has been growing [2]. The field of study on the synthesis, characterization, and uses of 2D carbides and nitrides known as MXenes have grown significantly since the synthesis of Ti_3C_2 was announced in 2011. $M_{n+1}X_nT_x$ is the generic formula for MXenes, there are far more conceivable structures than there are feasible metal atom ordering scenarios both in-plane and out-plane. It's increased even more by surface terminations [3].

The stability, electrical structure, and other physical and chemical properties of MXene are significantly impacted by surface terminations. Getting MXene materials with varied structural features and qualities effectively requires the controllable [4].

Among the myriad of terminal groups, hydroxyl (OH) and oxygen (O) functionalities stand out due to their prevalence and significant impact on the behavior of MXenes. Understanding the influence of these terminal groups on the structural and mechanical properties (elastic) of MXenes is essential for tailoring their properties to specific applications.

This study aims to delve into the nuanced effect of OH and O groups on the structural and mechanical characteristics of MXene Cr_2C, derived from MAX Cr_2AlC theoretically using the software Materials Studio, we seek to unravel the intricacies of how these terminal groups modulate the behavior of MXene Cr_2C at the atomic and macroscopic scales particularly on their mechanical properties.

This work is divided into two parts: the theoretical part and the computing part.

The theoretical part contains 3 chapters organized as follows:

- **CHAPTER I**: Under the title of "MAX and MXenes phases", include their history, an overview of their chemical composition, crystal structure of MAX phases, synthesis methods, the properties of MAX phases, and some potential applications for them.

- **CHAPTER II**: This chapter includes the mechanical (elastic) and structural properties of MXenes, the elastic stability condition and some other properties.
- **CHAPTER III**: This chapter generally covers the surface termination of MXene and their effects, include an introduction, overview which gives an understanding about it, their stability and the effect of surface termination on the mechanical properties of MXenes, and conclusion.

We find the practical part in the last chapter:

- **CHAPTER IV**: In this chapter, a specific type of MXenes called Cr_2C derived from MAX Cr_2AlC is studies by using CASTEP module from the software materials studio (MS) in order to see the effect of surface termination (OH) and (O) groups on the structural and mechanical (elastic) properties, then a general conclusion that summarize the main points, it's also offered insights, reflections and implications based on the findings results and discussions within the work and suggest avenues for further research and offer recommendations based on the findings.

THEORETICAL PART

CHAPTER I

MAX AND MXENES PHASES

I MAX AND MXENES PHASES

I.1 MAX PHASES:

I.1.1 History of the MAX Phases:

In Vienna in the 1960s, Nowotny's group discovered two 312 phases (i.e., Ti_3SiC_2 and Ti_3GeC_2) and most of the 211 phases (like Ti_2AlC, which were then called 'H-phases'). In the 1980s, Schuster, member of this group made the discovery of Ti_3AlC_2. These phases thereafter fell silent in the literature until a few articles by Barsoum and El-Raghy, published between 1996 and 1997, revealed that the majority of MAX phases exhibit an amazing blend of ceramic and metallic properties.

Following the discovery of Ti_4AlN_3, the first prototype of n=3 (or 413) phase in 1999, these phases were dubbed $M_{n+1}AX_n$ or MAX for short. Apart from the standard MAX phases, there are also hybrid structures (like $Ti_5Si_2C_3$ and $Ti_7Si_2C_5$).

Drexel University made the discovery of a new, huge family of 2D transition metal carbides and/or nitrides (MXene) in 2011 and 2012. The 'ene' suffix was added to mark the connection with grapheme and other 2D materials. MXenes are named because they are produced by etching the A elements (mostly Al) from there MAX counterparts.

The first documented chemically ordered quaternary 312 MAX phase was published in 2014. Not long later, researchers at the University of Poitiers in France verified the existence of more ordered Phases, or so-called o-MAX, extending to the 413 composition

In 2014, the first chemically ordered quaternary 312 MAX phase was reported. Shortly thereafter, the existence of other ordered phases (so-called o-MAX) was confirmed at the University of Poitiers in France and extended to the 413 composition [5].

I.1.2 Overview and the chemical composition of MAX phases:

The MAX phases, which are a broad family of over 100 phases made up of layered transition metal ternary carbides and/or nitrides have the general formula $M_{n+1}AX_n$, where n=1, 2 or 3 [6], in compounds containing two distinct M elements, the M element is a rare earth metal or a transition metal with a group number less than seven. A is an element having a group number between twelve and sixteen, is referred to as the A-element. In rare instances, the X-element may also be boron or selenium in addition to carbon or nitrogen [7].

The elements constituting the MAX phases are shown in (Figure I-1) [6]:

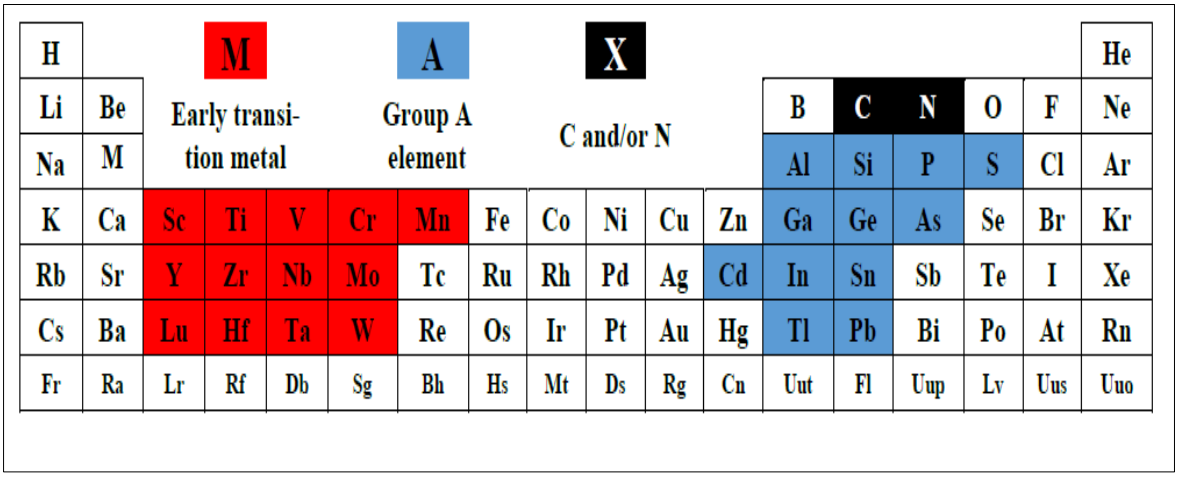


Figure I-1: Periodic table displaying the elements that make up the MAX phases: **A**: group A-element (blue), **X**: C and/or N (black), and **M**: early transition metal (red) [6].

These compounds have garnered a lot of attention lately because of their unique combination of metallic and ceramic properties, this make them potentially helpful in many applications. To date, about 60 phases have been synthesized out of the possibilities of three MAX phase elements. The most well-known are Ti_2AlC and Ti_3SiC_2 with the majority being 211 phases (n=1) [8].

I.1.3 The chemistry and crystal Structure of MAX phases:

Hexagonal symmetry characterizes common MAX phases with the space group P63/mmc. While the octahedra are centered by carbon and the M-elements occupy the octahedral edges, the X- and M-elements form layers of edge-shared octaherda. The M- and X-atoms are joined by strong covalent bonds. These octahedral layers may be single layers or several layers joined by common edges.

Most single atomic A-element layers with weak bonds to the M-atoms divide the M- and X- atom layers apart. For a number of n layers, the sum formula of MAX phases is hence $M_{n+1}AX_n$. In order to express the number of layers in a given MAX phase, the acronym (‘n+1’ ‘1’ ‘n’) is frequently utilized. A MAX phase with n=2, for instance, can be expressed as 312. To date, the highest value of n for MAX phase that has been seen is an experimental bulk molecule is 4. There are just two published works on MAX phases with n=4 [7].

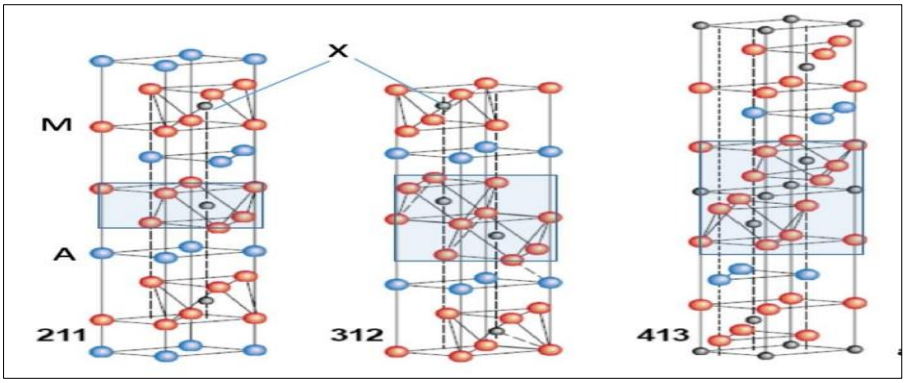


Figure I-2: Crystal structure of the 211, 312, and 413 MAX phases [9].

The 211, 312, and 413 MAX phases's hexagonal unit cells are displayed in (Figure I-2). The unit cells are made up of layers of A elements (e.g: Si or Ge) sandwiched between M6X octahedral (e.g: Ti6C). The number of M layers dividing the A layers in the three structures varies: there are two in the 211 phases, three in the 312 phases, and four in the 413 phases. The MAX phases' M6X edge sharing octahedral building block is identical to that of the MX binary carbides abs nitrides. There are two distinct M sites in the 312 and 413 MAX structures: M(1) and M(2), respectively, for sites that are next to A and those that are not. These sites are referred to as M(1) and M(2), in that order. Additionally, there are two non-equivalent X sites in the 413 structure: X(1) and X(2).

The A layer, which serves as a mirror plane, divides and twinned the MAX layers with respect to one another during the MAX phases. A high-resolution transmission electron microscopy (TEM) image taken of Ti_3SiC_2 along the $[11\bar{2}0]$ zone axis serves as an illustration of this (see Figure I-3). It's clear that the MAX phases are twinning, and that this causes the distinctive "zigzag" stacking of the phases. Because the MAX phases structures are anisotropic, the lattice parameters are often between a ~ 3 Å and c ~ 13 Å (211 phases), c ~ 18 Å (312 phases), and c ~ 23–24 Å (413 phases) [10].

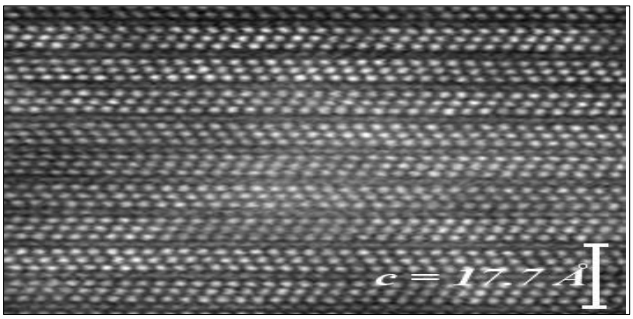


Figure I-3: High-angle annular dark field TEM image, acquired along the $[11\bar{2}0]$ zone axis of Ti_3SiC_2, showing twinning and the resulting characteristic "zig-zag" stacking of MAX phases [10].

I.1.4 Synthesis of MAX phases:

Both bulk materials and thin films can be produced for the MAX phases, as follows:

I.1.4.1 Bulk synthesis techniques:

Pressure-less sintering, hot pressing, hot isostatic pressing (HIP), self-propagating high temperature synthesis, and most recently microwave sintering are some of the bulk synthesis processes that have been employed to generate bulk MAX phases [6].

A. Pressure-less sintering:

One popular technique for making ceramics and pottery is sintering. Water and fine particles and combined to create a slurry that is shaped into the required shape. After that, the object is heated to high temperature, which causes the mixture to change into a more solid and compact form. We refer to the procedure as sintering. A component of the fine powders will become a liquid during sintering if its melting point is lower than the temperature at which sintering occurs. The procedure is therefore known as liquid-phase sintering (see Figure I-4.a). Solid-state sintering is the term used then there is no liquid phase during the sintering process (see Figure I-4.b) [6].

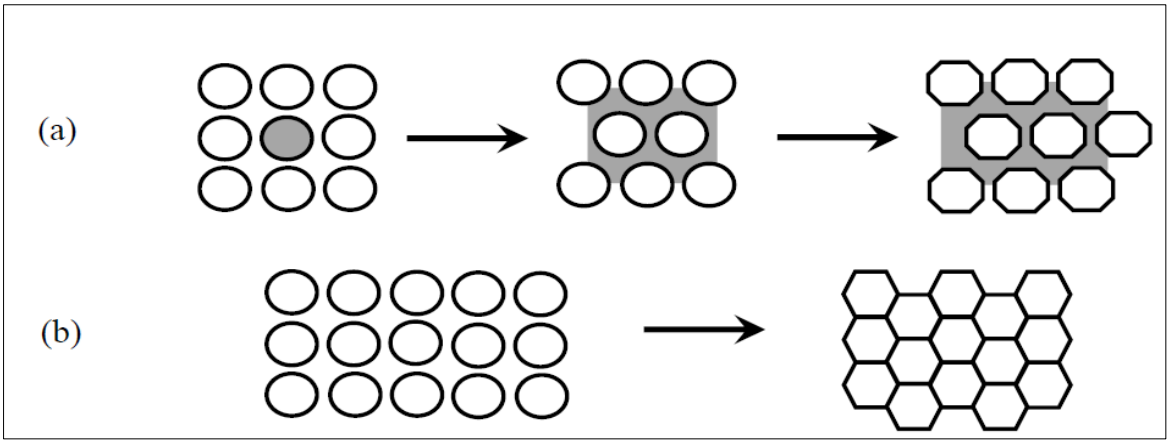


Figure I-4: **(a)** Liquid-phase sintering; **(b)** Solid-state sintering [6].

B. Hot pressing (HP):

High phase purity dense MAX phase samples are synthesized using HP, followed by heat treatment under argon or vacuum after being placed in a graphite die (see Figure I-5).

The maximum uniaxial pressure, which is usually up to 50 MPa, is dependent on the characteristics of the graphite and is applied throughout the whole heating cycle. Lower pressures (5-10 MPa) are utilized to encourage synthesis at temperatures up to 1000-1200°C,

while higher temperatures to promote densification. Maximum dwell temperatures typically range from 1200°C to 1700°c, and heating rates can reach up to 20°C/min. At maximum dwell temperature, isothermal holding periods can reach up to 10 hours. The primary benefit is that HP causes extremely pure MAX phases to fully density. But fundamental geometries (discs up to 5-4 mm additional shaping process before application) [11].

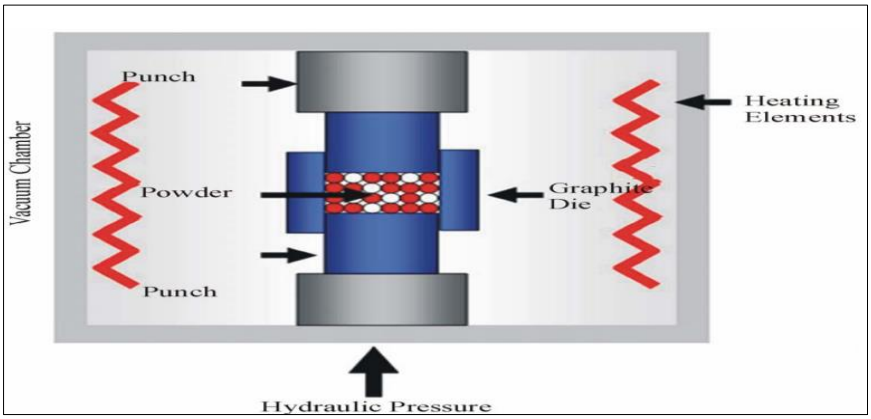


Figure I-5: Schematic diagram illustrating the hot pressing technique [12].

C. Hot isostatic pressing (HIP):

As HP, HIP produces very pure and dense MAX phases, but because of the isostatic pressure settings, there is no preferential orientation or texturing of the grains. Although the equipment and procedure for isotropic microstructures are more complicated. It's necessary to encapsulate the beginning powder in a suitable glass or metallic container before subjecting it to a thermal treatment for many hours at high pressures (100-300 MPa) under argon. Consequently, HIP is not often used even though the synthesis is feasible [11].

D. Self-propagating high-temperature synthesis (SHS):

Self-propagating high-temperatures synthesis (SHS) offers an efficient alternative to HIP, reducing energy consumption and facilitating the synthesis of multicomponent MAX phases [13].

Essentially, the precursor is combined evenly and compressed to produce superior green particles. The particles are then ignited in a vacuum by passing current through the tungsten wire, stopping oxidation. The highest temperature outdoors is approximately 1400 °C, and the typical combustion wave speed is 10 mm/s. the yield is the primary drawback, despite the process being quick and self-sufficient and producing vast amounts of powder. For the Ti-Al-C system, a number of beginning components have been investigated; however, it is challenging to prevent the presence of carbides and other second phases because of the rapid

burning rate and thermal gradient. The primary drawbacks are the second phase's high content and the potential need for grinding [11].

E. Microwave sintering (MW):

MW is a direct energy delivery technique that provides high heating rates, a specific heating zone, and pressure-free heating. The initial precursors are heated in an argon environment for up to 30 min, with heating rates of up to 200°C/min and maximum temperatures of 850°C to 1480°C. The improved species diffusion resulting from their contact with the microwaves and the reported drop in activation energy, 233 KJ/mol for the production of Ti_3SiC_2 are linked to the sintering temperature reduction.

The synthesized pellets have a grain size range of 1-10μm and high purity of up to 97.5%, but are porous and require a milling phase for powder production, despite potential drawbacks [11].

I.1.4.2 Thin film synthesis techniques:

Here, we provide a brief overview of the several growth methods used for the deposition of thin MAX Phases films, including cathodic arc deposition, magnetron sputtering, chemical vapor deposition, and pulsed laser (CVD), and pulsed laser deposition.

Generally, CVD needs temperatures above 1000°C, but isn't very successful since it uses a lot of solution-based precursors that leave a lot of residue on the surface. To grow MAX phase films, high power dc or radio frequency (rf) magnetron sputtering has been frequently employed. Its benefit is that each element and the target compositions may be controlled since separate target sources are employed for sputtering. Films are usually developed using this process at temperatures between 700–1000°C. Reactive magnetron sputtering, which use N_2 as a source, has also been used in certain instances to deposit the films. Certain MAX phase thin films can be grown using the cathodic arc deposition approach due to its high ionization, allowing growth at a low substrate temperature of 500°C. The PLD technique, utilizing high-energy vapor phase deposition, has been successfully used to grow various MAX phase thin films. Here, one can use a single MAX phase target can be ablate using a high energy pulsed laser beam (eV). Generating plasma and allowing true stoichiometric transfer, resulting in high-potential single phase epitaxial films grown at 700°C [14].

I.1.5 MAX phases property:

Particularly metallic nature resulting from the strong covalent and ionic connections between M and X atoms, and the weaker M and A atom bonds, particularly under shear stress. The bond of M-A offers features of electrical and thermal conductivity, whereas the bond of M-X results a highly elastic stiffness of MAX phases. As seen in (Figure I-6), these linkages combine to give the MAX phases their unique metallic-ceramic properties. They have many properties, including significant thermal and electrical, plasticity deformation at high temperatures, and resistance to thermal shock (about to 1400°C). In terms of thermal expansion, they are similar to ceramics since they have a high Young's modulus and are relatively light [15].

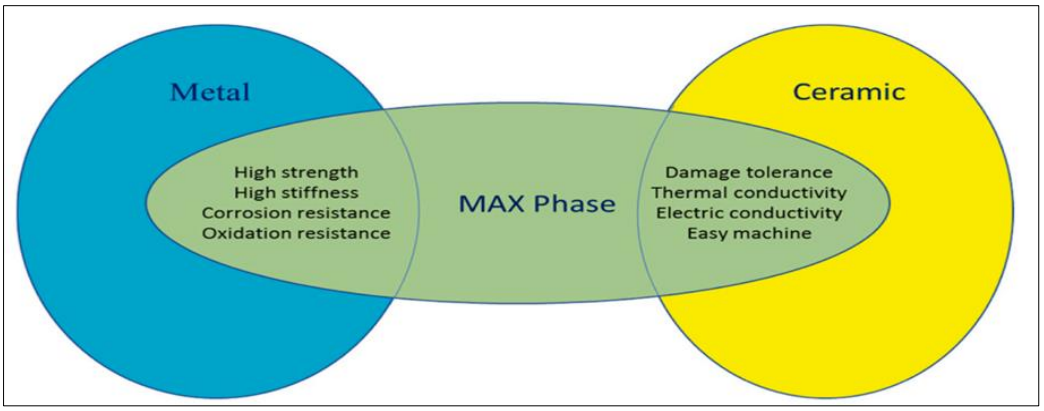


Figure I-6: Characteristics of the MAX phase ceramics [15].

MAX- Phases have unique mechanical properties and greater customization potential due to their three distinct intrinsic constituent, unlike their binary counterparts, MX carbides or nitrides. The composite material is strengthened and dislocation motion (slide plane movement) is prevented compositions. Ceramics that are elastically stiff have tiny expansion coefficients, high temperatures. MAX phases also have wear-resistant, low-friction, and machinable surface. On the other hand, the MAX phases are resistant to fatigue, oxidation, creep, corrosion, and fractures. As a result, the MAX phases combining metal and ceramic properties, provide and electronic characteristics of Nano-scale constituent layers [15].

I.1.6 Potential applications of MAX phases:

After obtaining a license for Drexel University's MAX technology in the late 1990s, Kanthal Corp. Created Ti_2AlC heating elements and explored additional possible uses. These heating components exhibited exceptionally stable behavior due to a protective, adherent oxide scale, even after being cycled over 8000 times from ambient temperatures to 1350°C.

Ti_2AlC was suggested as gas burner nozzles due to its exceptional performance in corrosive environments, effectively replacing the severely degraded steel nozzles [11].

I.2 MXENES PHASES:

I.2.1 History of MXenes Phases:

In 2004, the discovery of single and few-layer grapheme led to the exploration of 2D materials beyond grapheme, including graphite-like hexagonal boron nitride, dichalcogenides, and layers oxides. This led to the development of 2D Si (silicone), Ge, Sn and several other materials, indicating a potential expansion of the 2D materials family.

A significant class of materials, early transition metal carbides and nitrides have high metallic electrical conductivity, high hardness, and great chemical stabilities. They have been investigated for decades as bulk ceramic materials, primarily for use in cutting tools and high temperature application.

Barsoum and El-Raghy made single phase pure samples of Ti_3SiC_2 in 1996, demonstrating its machinability and excellent conductivity. They discovered 50 phases, including Ti3SiC and Ti_4AlN_3, later referred to as MAX phases [16].

In 2011, Naguib and coworkers demonstrated that 3D Nano-laminate MAX phases could be exfoliated into 2D crystals using chemical etching and sonication techniques. Since then, 30 transition-metal carbides and nitrides, called MXenes, have been reported with various chemical compositions and orders. The thickness of the MXene monolayer varies with the n index and terminal group nature [17].

I.2.2 Overview and the Chemical composition of MXenes phases:

Transition metal carbides and nitrides, sometimes referred to as MXenes (pronounced “maxenes”), a rapidly expanding class of 2D materials. The general formula of $M_{n+1}X_nT_x$ describes how n+1 (n=1−3) layers of early transition metals (M, elements in blue in Figure I-7) are interleaved with n layers of carbon or nitrogen (X, elements in gray in Figure I-7). The surface terminations that are bonded to the outer M layers, such as O, OH, F (elements in orange in Figure I-7) are represented by the symbol Tx in the formula.

Atomic schematics of three types of MXenes are displayed at the bottom of (Figure I-7) [18].

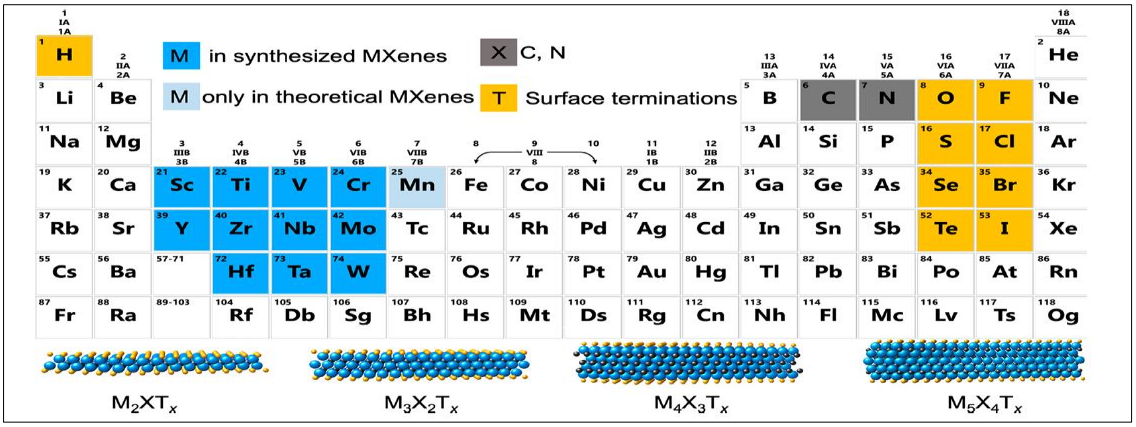


Figure I-7: Periodic table displaying MXenes compounds. The components of MXenes are color-coded. The bottom section displays the schematics of four common MXenes structures [3].

Nevertheless, oxidation can readily break down MXene's structure because of the abundance of exposed metal atoms on its surface. Errorable lamellar stacking during preparation and application is another problem with MXene. Inadequate mechanical strength, poor multiplier performance, poor solubility in non-polar or weakly poor polymers, and poor environmental stability...etc [4].

I.2.3 Synthesis of MXenes phases:

The bulk MAX phases, which are physically defined by $M_{n+1}X_n$ layers interspersed with one layer of group 11-16 A-element atoms, are the source of the majority of experimentally produced MXenes. Strong ionic/covalent M-X bonds within the $M_{n+1}X_n$ layers and weaker metallic M–A bonds between the layers together (see Figure I-8). Certain non-MAX phases that have been exfoliated into MXenes, like Mo_2CTx from Mo_2Ga2C, exhibit comparable M–X and M–A bonding. These variations in binding strength enable the cleaving of M–A bonds during exfoliation, preserving the $M_{n+1}X_n$ layers. [19].

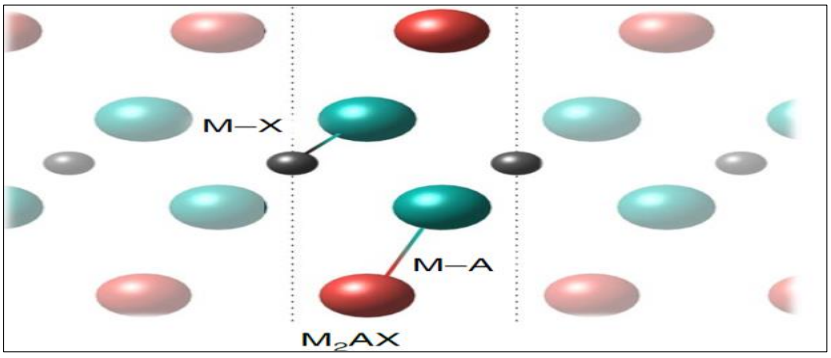


Figure I-8: M–X and M–A bonds schematic in a MAX phase, with M_2X layers positioned between layers of a single A atom. Green, red and black spheres represent **M**, **A** and **X**, in that order [19].

I.2.4.1 HF/Fluoride etching:

One of the most effective etchants for phase exfoliation is hydrofluoric acid (HF). The two most popular HF-based etching techniques for creating MXenes are in situ HF etching and direct HF etching. Compared to the direct HF etching method? In situ HF is typically generated by less aggressive etchants like HCL and LiF mixture and other Fluoride-containing acids. As a result, MXene flakes with larger lateral dimensions, fewer flaws and higher electrical conductivity can be created. The "A" layer of the MXene precursors is etched using HF as an etch to create multilayered MXene Nano-sheets through the subsequent reaction, which forms the basis of this process [2]:

$$\mathbf{Mn + 1AXn + 3HF \rightarrow AF3 + 1.5H2 + M\,n + 1Xn} \qquad \mathbf{I.1}$$

$$\mathbf{M\,n + 1Xn + 2H2O \rightarrow M\,n + 1Xn(OH)2 + H2} \qquad \mathbf{I.2}$$

$$\mathbf{M\,n + 1Xn + 2HF \rightarrow M\,n + 1XnF2 + H2} \qquad \mathbf{I.3}$$

Equation (I.**1**) show that the M-A bond, which is weaker than the M-X bond, is a metal bond in MAX-phase ceramics. HF combines with the A layer elements in the MAX phase to produce AF_3, H_2, and the associated $M_{n+1}X_n$ phase because of the difference in binding energies. Nevertheless, $M_{n+1}X_n$, which is devoid of elements in the A-layer, combines with the nearby HF or water to generate $M_{n+1}X_n(OH)_2$, which includes functional groups for OH or/and F, as stated in equations (I.2)and(I.3) The structure following surface functional group modification and the representative steps of Ti_3C_2Tx MXene production from Ti_3AlC_2 are depicted in (Figure I-9) [4].

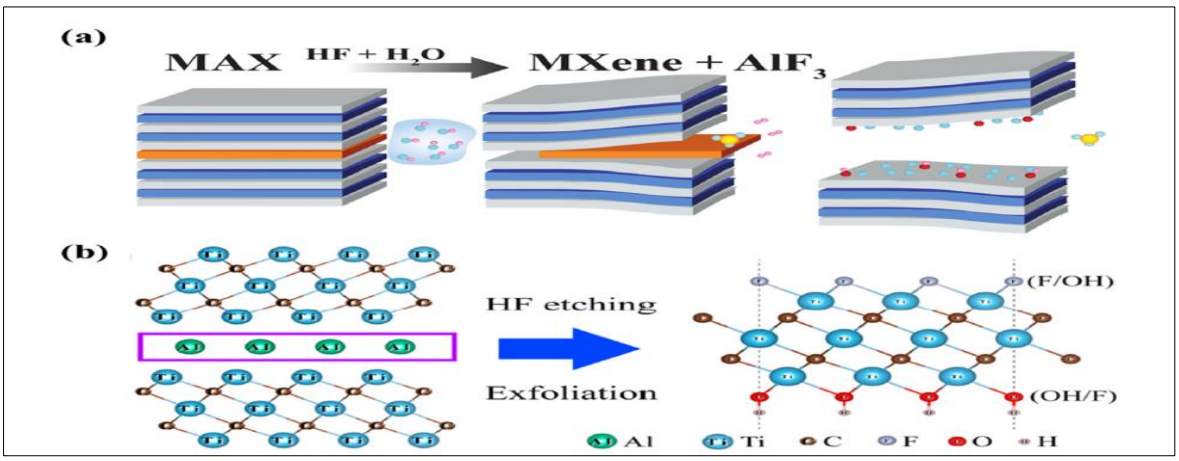


Figure I-9: **(a)** Schematic diagram of the synthesis of MXene by HF etching. **(b)** The synthesis and structure diagram of Ti_3C_2Tx MXene [4].

Using acid/fluoride salt solutions to etch MAX-phase ceramics such as HCl/LiF, HCl/NH_4F, HCl/FeF_3, and H_2SO_4/LiF is another reactive technique. As seen in (Figure I-10). LiF powder was added to strong HCL, and it was thoroughly dissolved by stirring. Then, Ti_3AlC_2 MAX powder was gradually added to the LiF/HCl dispersion, and the etching was done for 24 hours at 35°C with magnetic stirring in a water bath. Deionized water was used to repeatedly wash the resultant combination until a black supernatant with a pH of around 5 was obtained. The mixture was subjected to a mild ultrasonic treatment, and the resulting supernatant was collected and freeze-dried to produce MXene powder containing functional groups (O), (OH), and (F) [4].

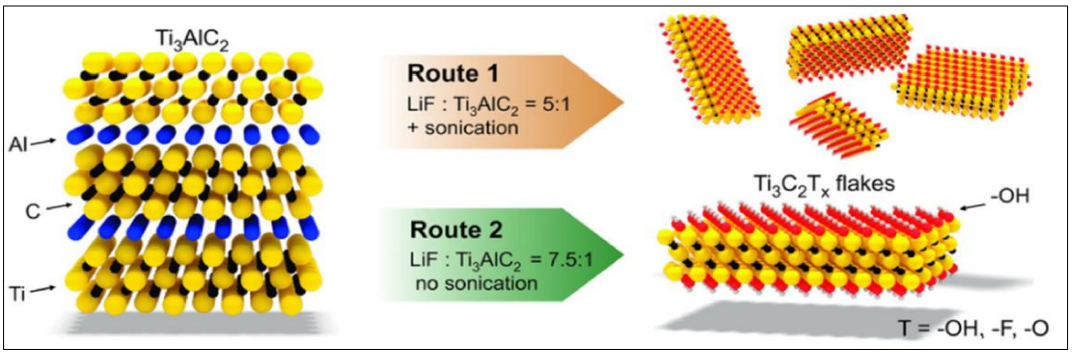


Figure I-10: Schematic diagram of the synthesis of Ti_3C_2Tx MXene by fluoride etching [4].

I.2.3.2 Molten salt etching method:

Researchers are exploring alternatives to HF-etching, with molten-salt etching being a prominent method. J, Liew et al [2]. Synthesized titanium nitride MXene using molten fluoride salt etching, a safer alternative to traditional methods. By using a replacement reaction mechanism, MAX phases are etched by heating them to high temperatures in a molten lewis acid salt. Molten salt etching broadens the variety of MAX-phase precursors that may be employed, provides significant options for adjusting the surface chemistry and properties of MXene, and make it possible to produce new 2D materials that are challenging or perhaps impossible to generate using current synthesis methods.

However, due to the absence of OH-terminal groups, molten salt etching produces MXene clays that are not colloidally stable. For this reason, J, Liew et al [2]. Created water-dispersible $Ti_3C_2T_x$ by employing thin fluoride, or SnF_2. By heating a mixture of Ti_3AlC_2 and SnF_2, delamination by sonication, washing, and intercalation with KOH and DMSO, respectively, they created $Ti_3C_2T_x$ (see Figure I-11).

MXenes with water-dispersible properties are easily processed in water-based inks, coatings, and sprays using SnF_2 etchant and KOH washing, resulting in stable aqueous dispersions. The synthesized $Ti_3C_2T_x$ has the typical accordion structure, which indicates that the aluminum was successfully etched from the MAX phase (Figure I-11A). However, (Figure I-11B-C) show the unusual presence of crystalline structures intercalating the layers, which were thought to be SnF_2 and AlF_3 salts formed by SnF_2 diffusing between the layers during the etching process and forming AlF_3. Their MXene clay yield was approximately 82%, while their MXene Nano-sheet yield was 10%.

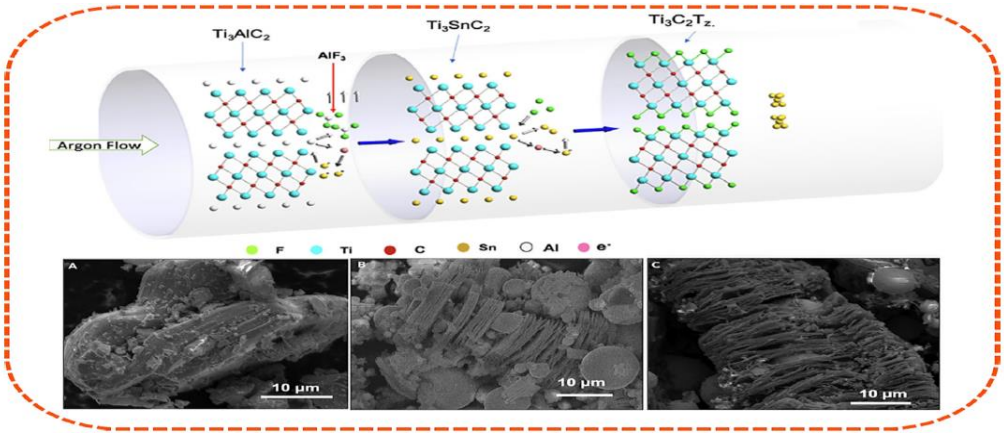


Figure I-11: Schematic of the reaction setup used for molten salt etching in a tube furnace under argon flow to minimize the interference of oxygen during etching. FESEM images of **(A)** Parent Ti_3AlC_2 MAX phase, **(B)** $Ti_3C_2T_x$ before KOH wash (freeze-dried), **(C)** $Ti_3C_2T_x$ after KOH wash (freeze-dried) [2].

I.2.4 Applications of MXenes:

Functional MXenes can offer more electrochemically actives sites and better electronic structure than the original 2D MXenes demonstrating enhanced performance. Because of their ideal surface, plenty of active sites, greater diffusion space, and superior mechanical properties, functional MXenes-which can be produced through a variety of techniques such as tuning MXene terminations, heteroatom doping, enlarging interlayer space, or hybridization with polymers-have been used in the fields of energy storage, catalysis, sensors, EMI shielding, and MA.

The ability to customize MXene surface functionalization for various application circumstances is made possible by its diversity. Novel gadgets are also possible by their tiny profile and processability as inks [20].

I.2.4.1 Energy storage:

Low electron transport barriers, a high specific surface area, a short path of ion diffusion, and the thickness of the MXene atoms crystalline structure are the results of these factors. A recent study by energy experts looked into how to enhance energy storage devices (ESDs) over the next 50 years by using MXene and materials based on MXene. Because of their innate qualities, MXene are attractive options for polymer electrolytes because they allow for the incorporation of high ionic conductivities. The main benefit of MXene as a material for energy storage is its exceptionally high conductivity. The intrinsic features of MXenes are superior to those of typical electrode materials utilized in energy storage systems. Because of MXene's metallic properties, which enable it to conduct electrons efficiently, batteries and super-capacitors rely on its increased conductivity [21].

I.2.4.2 Electromagnetic interference shielding:

Electromagnetic interference (EMI) is a byproduct of electronic device operation that effects the environment. Shielding is necessary because EMI is increasing as a result of smaller, faster-operating electronic gadgets. For materials to be used in electrical equipment, they must also be flexible and lightweight with strong shielding qualities. Mo_2TiC_2Tz, $Mo_2Ti_2C_3Tz$, and Ti_3C_2Tz vacuum-filtered films were examined. Throughout the GHz electromagnetic frequency band, they all demonstrated exceptional EMI shielding properties. The reaction was superior to that of synthetic and other grapheme-based composites of the same thickness, as well as thin Cu layers. But the main benefit of MXene over metal shields is how simple it is to create them in extremely thin form. In the THz region, thin Ti_3C_2Tz MXenes on Nano-slot antennas also exhibit significant promise [22].

I.2.5 Conclusion:

In conclusion, MAX phases and MXenes represent promising avenues for materials research and application development. Their unique combination of properties opens up opportunities for innovation across various industries, from electronics to energy storage and beyond.

the development of MXenes has seen rapid progress in recent years, with researchers exploring novel synthesis methods, optimizing their properties, and investigating their applications in diverse fields, which indicates the interest of scientists and researchers in this new type of material that will create an insurgency in the future in various fields.

CHAPTER II

STRUCTURAL AND MECHANICAL PROPERTIES OF MXENES

II STRUCTURAL AND MECHANICAL PROPERTIES OF MXENES

II.1 Introduction:

MXenes, a broad class of 2D materials with significant applications in a variety of fields, and derived from nitride, carbides, or caronitrides of transition metals. In this regard, customizing MXenes' diverse attributes [23].

MXenes have a wide and variable surface interaction due to the number of electrons connected to transition metal atoms. The MAX phase, etching and raw materials, delamination and etching techniques, and mechanical, electrical, chemical, magnetic, surface, thermal, and redox properties of MXenes are among the intriguing aspects that are regulated by these factors. Additionally, by modifying its composition, adding new "M" and "X" elements, and changing the surface terminal functions, the properties of MXenes can be adjusted for suitable applications. Lately, MXenes' characteristics have been described by theoretical investigations that make use of computer techniques [24].

II.2 Structural properties:

II.2.1 Structure of MXene:

The A element can be extracted from the parent MAX phases to create the structure of pristine MXenes. (Figure II-1) shows the structure of typical virgin MXenes with the basic formula $M_{n+1}X_n$ (n=1, 2, 3). The resulting MXenes are hexagonal in accordance with the symmetry of the precursor MAX phases. The X layers are alternately sandwiched between the M layers in a layered structure made up of the atoms. Similarly, a hexagonal symmetry is present in the o-MXenes with the general formula M'2M"X2 or M'2M"2X3 (see Figure II-1). The M' element is the only element that forms the outside layers of o-MXenes, whereas the M'' element forms the inner layer or layers.

Either 2D $M_{1.33}X$ systems with ordered divacancies or 2D i-MXenes with the general formula (M'2/3M"1/3)2X are produced by the exfoliation of the in-plane ordered MAX phases. Their pristine structures are illustrated in (Figure II-1).

Each layer containing two distinct transition metal elements causes the bigger M'' atoms to shift slightly out of plane from their normal placements. This displacement causes the system symmetry to shift from hexagonal to monoclinic [17].

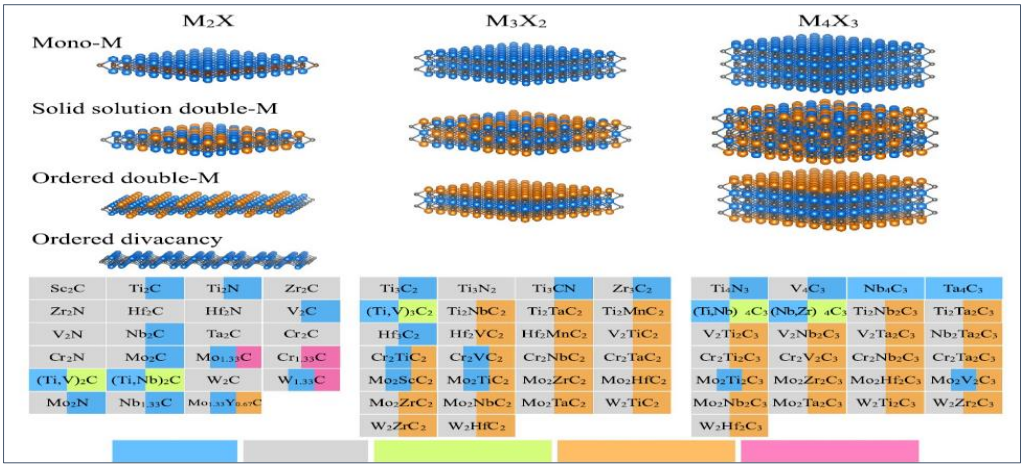


Figure II-1: The Chemical versatility of all currently available MXenes systems, including conventional $M_{n+1}X_n$ (n=1, 2, 3), double-M solid solutions, out-of-plane ordered, in-plane ordered double-M, and divacancy ordered MXene systems [17].

Current MXene structures can be categorized into four types: ordered double-transition metal (M) MXenes, like $(Cr_2V)C_2$ and $(Mo_2Ti_2)C_3$; ordered divacancy MXenes, like $Mo_{1.33}C$ and $W_{1.33}C$ (see Figure II-2A, B); mono-transition metal MXenes, like Ti_2C and Nb_4C_3; and solid solution MXenes, like $(Ti, V)_2C$.

Apart from the typical 2D MXenes structure (Figure II-2A), there are one-dimensional (Figure II-2B, C), three dimensional (Figure II-2D), and quasi-zero-dimensional (Figure II-2E) structures. MXenes of one-dimensional structure have been investigated less than those with 2D structure, which has been the subject of much research [25].

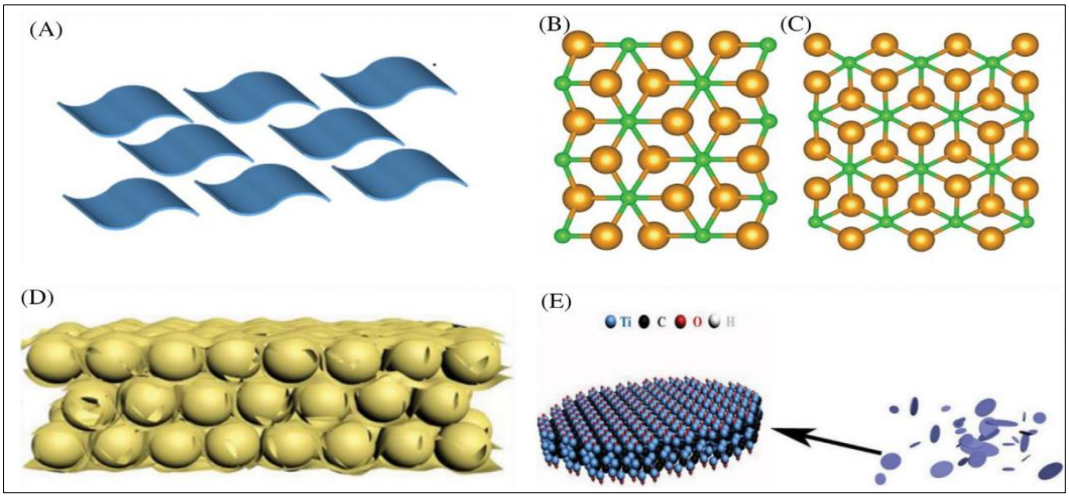


Figure II-2: The 1D, 2D, 3D, and 0D structures of MXenes. **(A)** Two-dimensional structure of MXene Nano-sheets. Top view of the geometric structures of **(B)** zigzag and **(C)** armchair Ti2C Nano-ribbons. Yellow and green balls indicate Ti and C atoms, respectively. **(D)** The 3D M-Ti_3C_2Tx film. **(E)** The nonoxidized MXene-Ti_3C_2Tx quantum dots (NMQDs-Ti_3C_2Tx) prepared by micro-explosion method [25].

II.2.2 Crystal and atomic structure of MXenes:

The hexagonal lattice of the MXene monolayer sheet exhibits six-fold symmetry. From a top view, it possesses a rhombus unit cell similar to grapheme, as shown by the dotted lines in (Figure II-3a) (upper panel). The MXene monolayer, seen from the side, is made up of trilayer sheets with one X layer sandwiched between two M transition metal layers. This produces M_2XF_2, M_2XO_2, and $M_2X(OH)_2$ and is caused by the common six-coordination seen in transition metal ions. The hollow locations of the M_2X surfaces can be divided into two categories when the functional groups are taken into consideration: A and B (Figure II-3a, lower panel). X atoms are located beneath type B sites, whereas in type A, they are not present between the M layers and the hollow sites. As a result, two energetically stable terminal group attachment arrangements are shown. A hollow site, A (Figure II-3b), can be occupied by two functional groups in one configuration, while a hollow site, B, can be inhabited by two functional groups in another configuration.

Since the functionalization reactions demand negative formation energies, functionalized MXenes are thermodynamically stable; in fact, the surfaces of completely functionalized MXenes are thermodynamically more favorable than those of partially functionalized MXenes [26].

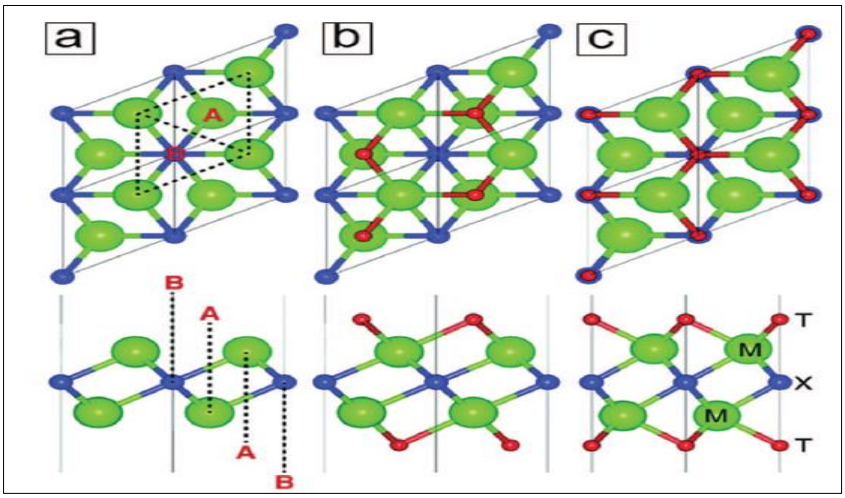


Figure II-3: Crystal structures of two-dimensional (2D) M2X MXenes. **(a)** The Ti_2C MXene model comprises a rhombus unit cell (dashed line) with hexagonal symmetry (top view). It consists of trilayer configurations where the C atomic layer is sandwiched between two Ti atomic layers (bottom panel). **(b)**, **(c)** MXene models with two different surface termination group configurations [26].

II.2.3 Types of structures:

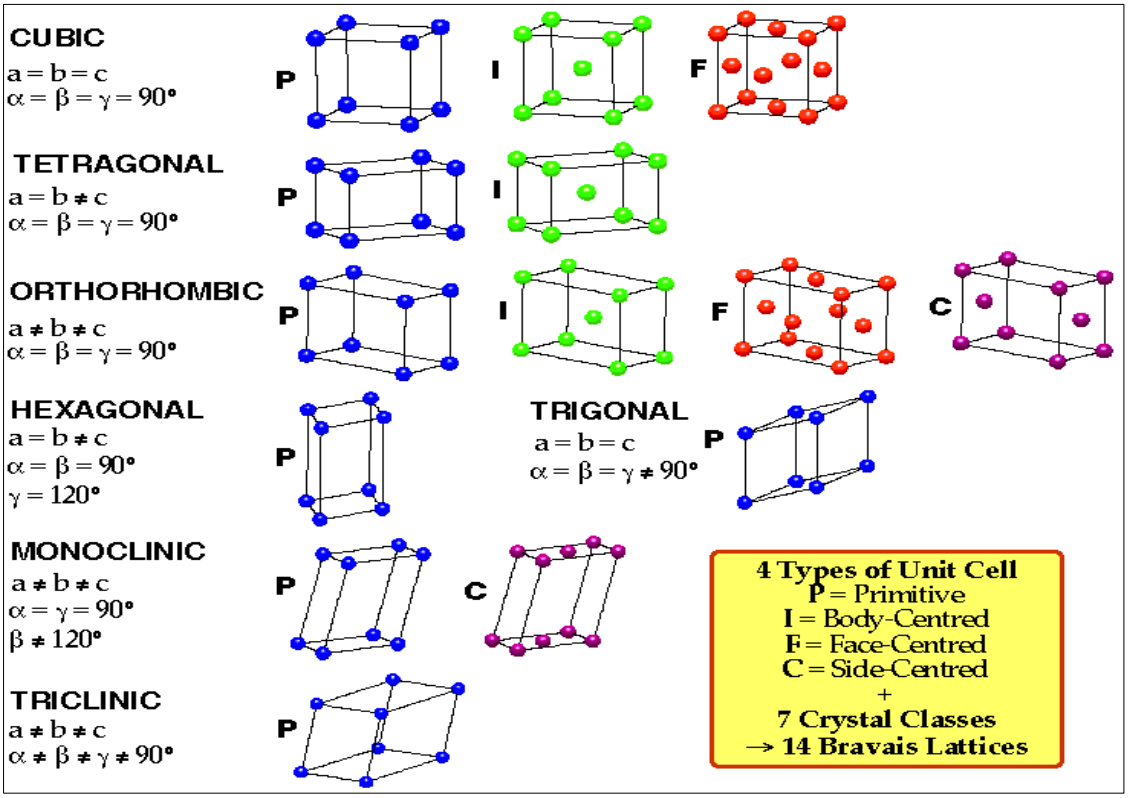


Figure II-4: The 14 bravais-lattices in 3d [27].

Table II-1: Classification of crystal families and systems. Centering type, Laue group, Hermann-Mauguin point-group symbols, and space-group numbers (SGN) [28].

Crystal family	*Crystal System*	*Centering Type (s)*	*Laue group*	*Point group classes*	*SNG*
Cubic	Cubic	*P, F, I*	C_I	432, $\bar{4}3m$, $\frac{4}{m}\bar{3}\frac{2}{m}$	207-230
			C_{II}	23, $\frac{2}{m}\bar{3}$	195-206
Hexagonal	Hexagonal	*P*	H_I	622, 6mm, $\bar{6}2m$, $\frac{6}{m}\frac{2}{m}\frac{2}{m}$	177-194
			H_{II}	6, $\bar{6}$, $\frac{2}{m}$	168-176
	Trigonal	*P, R*	R_I	32, 3m, $\bar{3}\frac{2}{m}$	149-167
			R_{II}	3, $\bar{3}$	143-148
Tetragonal	Tetragonal	*P, I*	T_I	422, 4mm, $\bar{4}2m$, $\frac{4}{m}\frac{2}{m}\frac{2}{m}$	89-142
			T_{II}	4, $\bar{4}$, $\frac{4}{m}$	75-88
Orthorhombic	Orthorhombic	*P, C, F, I*	O	222, mm2, $\frac{2}{m}\frac{2}{m}\frac{2}{m}$	16-74
Monoclinic	Monoclinic	*P, C*	M	m, 2, $\frac{2}{m}$	3-15
Triclinic	Triclinic	*P*	N	1, $\bar{1}$	1 and 2

II.3 Mechanical properties:

MXene's 2D stiffness generally higher for $–O_2$ terminations, whereas it decreased slightly for F_2, $(OH)_2$ and Cl_2 terminations (see Figure II-5) [4].

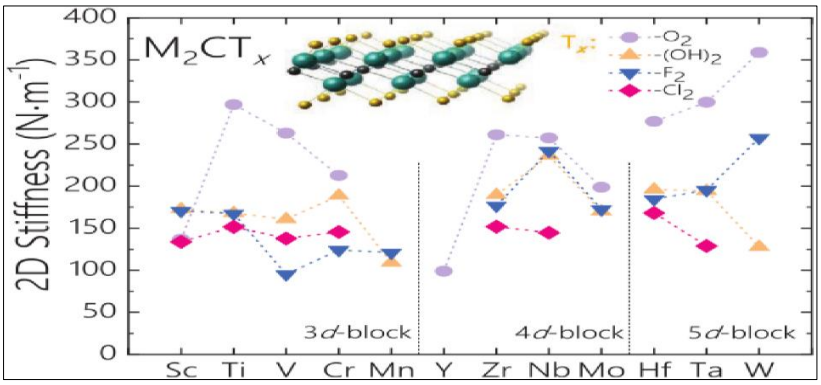


Figure II-5: Predictions on the mechanical 2D stiffness for terminated M_2XTx MXene for different surface terminations including O_2, F_2, $(OH)_2$, and Cl_2 [4].

During analysis, it is done to assess how M, X, and Tx affect the real bond properties in the structure of MXenes using the 2D stiffness. To describe the mechanical reaction of MXenes under loading circumstances in structural applications, the 3D elastic modulus is required. An extra variable in the process is the monolayer thickness, which links the 3D elastic modulus to the 2D stiffness. It is demonstrated that a rise in "n" of $Ti_{n+1}X_n$ increases the 2D stiffness. But for "n=1, 2, and 3" in bare $Ti_{n+1}C_n$ the elastic modulus shows a distinct trend. Decreasing from 604 GPa to 454 GPa, and 479 GPa respectively (Figure II-6 a). More evidence is provided regarding the impact of terminating M_2XTx MXenes' higher monolayer thicknesses on the elastic modulus in (Figure II-6 b) [29].

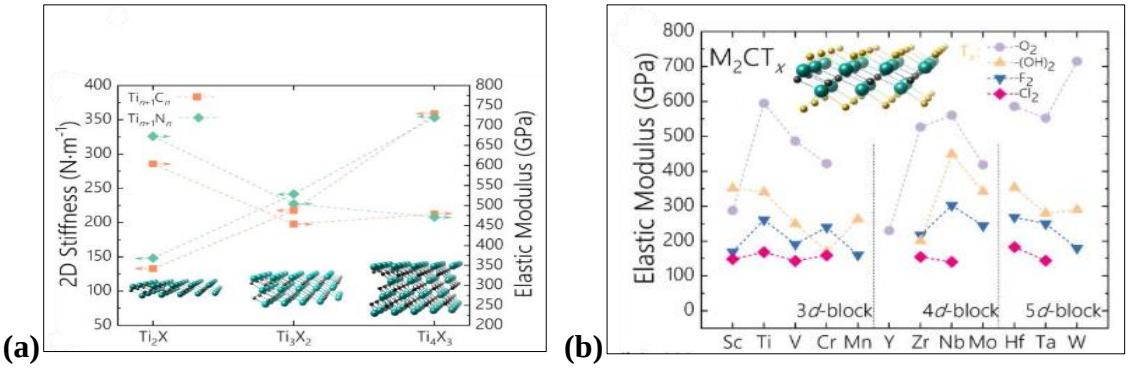


Figure II-6: (a): 2D stiffness and elastic modulus of Tin+1Xn (X = C, N) MXene, which illustrate the effect of increasing flake thickness (n) on MXenes' mechanical stiffness. **(b)**: Prediction of the elastic modulus of terminated MXenes, which illustrates the effect of increased monolayer thickness due the surface terminations on the stiffness trends in MXene. [29]

II.3.1 Elastic properties:

II.3.1.1Strength and Stress-Strain Curve:

The ability of a material to withstand forces applied from outside without cracking or giving way is referred to as its strength. The ultimate strength (D) of a material is the highest stress it can sustain before breaking. The link between stress and strain is depicted in (Figure II-7). The material's yield strength and ductility are described by the stress and strain curve that was acquired during the tensile test. Figure II-7 indicates that a material's elasticity-that is, its ability to return to its original dimension-would be preserved up to its elastic limit, after which plasticity would take over. When the material surpasses the ultimate stress point (D), the specimen begins to exhibit necking. To achieve ultimate tensile strength, strain hardening is maintained in between yield points. A substance accurately obeys Hooke's law up to a proportionate limit. The stress and strain curve is used to determine the material's Young's modulus. The A-B range is measured as the elastic limit. Strength is the capacity of a material to withstand loads without experiencing undue failure or distortion. It is also the capacity of a material to respond equally to applied forces (tensile, compression, and shear) without rupturing. Put simply, strength is the material's maximal resistance to deformation. Comparably, a material's tenacity is its capacity to withstand rupture brought on by a tensile force [30].

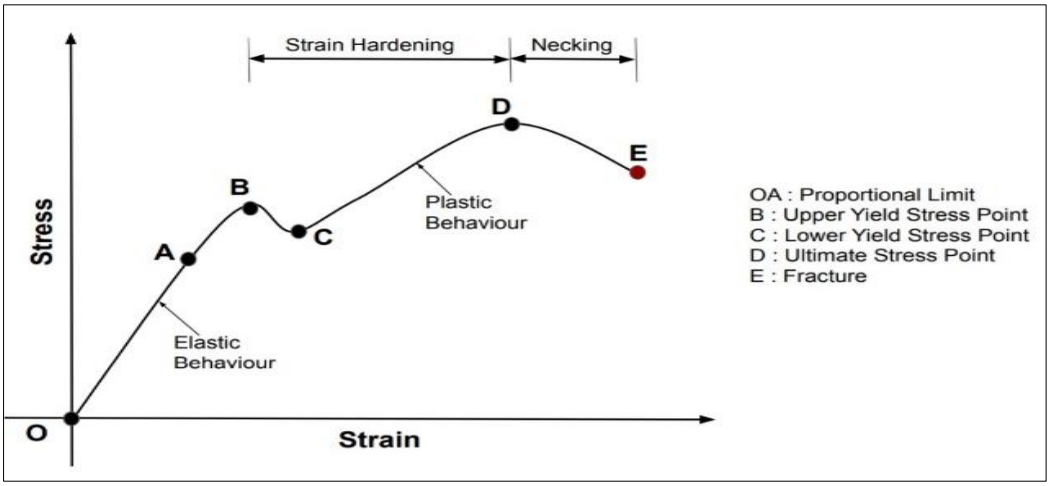


Figure II-7: Stress- strain relationship curve [30].

- **Elasticity:**

Materials have the ability to return to their original shape after deformation as long as the external forces are eliminated. A spring's extension, or compression, serves as an

example. Materials used to make tools and machinery would benefit from having this feature. Rubber is less elastic than steel. Elasticity is a material's properties. Elasticity is shown by the proportional limit and elastic limit. Another name for it is nonpermanent deformation. It has two sub properties that make up this elastic era. They are the elastic limit and the proportional limit. The highest stress at which a material will continue to exhibit a fully uniform rate of strain to stress is known as the proportional limit [30].

- **Plasticity:**

It is a material's capacity to permanently deform to some extent without breaking or failing. This indicates a material's ability to permanently deform when a load is applied. Plastic deformation only occurs when the shear stress on the slip plane reaches a critical value, which is the point at which the slipping process exceeds the elastic range. Even once the pressures are removed, the slipping-caused displacement is irreversible, and the crystal planes don't revert to their initial positions [30].

II.3.1.2 Hooke's Law:

The generalized Hooke's Law for a linear elastic material is written:

$$\begin{bmatrix} \boldsymbol{\sigma_1} = \boldsymbol{\sigma_{xx}} \\ \boldsymbol{\sigma_2} = \boldsymbol{\sigma_{yy}} \\ \boldsymbol{\sigma_3} = \boldsymbol{\sigma_{zz}} \\ \boldsymbol{\sigma_4} = \boldsymbol{\sigma_{yz}} \\ \boldsymbol{\sigma_5} = \boldsymbol{\sigma_{xz}} \\ \boldsymbol{\sigma_6} = \boldsymbol{\sigma_{xy}} \end{bmatrix} = \begin{bmatrix} \boldsymbol{C_{11}} & \boldsymbol{C_{12}} & \boldsymbol{C_{13}} & \boldsymbol{C_{14}} & \boldsymbol{C_{15}} & \boldsymbol{C_{16}} \\ \boldsymbol{C_{21}} & \boldsymbol{C_{22}} & \boldsymbol{C_{23}} & \boldsymbol{C_{24}} & \boldsymbol{C_{25}} & \boldsymbol{C_{26}} \\ \boldsymbol{C_{31}} & \boldsymbol{C_{32}} & \boldsymbol{C_{33}} & \boldsymbol{C_{34}} & \boldsymbol{C_{35}} & \boldsymbol{C_{36}} \\ \boldsymbol{C_{41}} & \boldsymbol{C_{42}} & \boldsymbol{C_{43}} & \boldsymbol{C_{44}} & \boldsymbol{C_{45}} & \boldsymbol{C_{46}} \\ \boldsymbol{C_{51}} & \boldsymbol{C_{52}} & \boldsymbol{C_{53}} & \boldsymbol{C_{54}} & \boldsymbol{C_{55}} & \boldsymbol{C_{56}} \\ \boldsymbol{C_{61}} & \boldsymbol{C_{62}} & \boldsymbol{C_{63}} & \boldsymbol{C_{64}} & \boldsymbol{C_{65}} & \boldsymbol{C_{66}} \end{bmatrix} \times \begin{bmatrix} \boldsymbol{\varepsilon_1} & \boldsymbol{\varepsilon_{xx}} \\ \boldsymbol{\varepsilon_2} & \boldsymbol{\varepsilon_{YY}} \\ \boldsymbol{\varepsilon_3} & \boldsymbol{\varepsilon_{zz}} \\ \boldsymbol{\varepsilon_4} & \boldsymbol{\varepsilon_{yz}} \\ \boldsymbol{\varepsilon_5} & \boldsymbol{\varepsilon_{xz}} \\ \boldsymbol{\varepsilon_6} & \boldsymbol{\varepsilon_{xy}} \end{bmatrix} \quad \textbf{II.1}$$

The anisotropic elasticity equations can be expressed in matrix form thanks to this useful notation, which has only one subscript for each of the stress and strain, numbered from 1to 6. The stiffnesses are the C_{ij} of 36. The stiffness matrix is the matrix of stiffnesses. You can flip this matrix to explicitly provide the strains in terms of the stresses [31]:

$$\begin{bmatrix} \mathcal{E}_1 \\ \mathcal{E}_2 \\ \mathcal{E}_3 \\ \mathcal{E}_4 \\ \mathcal{E}_5 \\ \mathcal{E}_6 \end{bmatrix} = \begin{bmatrix} \boldsymbol{S_{11}} & \boldsymbol{S_{12}} & \boldsymbol{S_{13}} & \boldsymbol{S_{14}} & \boldsymbol{S_{15}} & \boldsymbol{S_{16}} \\ & \boldsymbol{S_{22}} & \boldsymbol{S_{23}} & \boldsymbol{S_{24}} & \boldsymbol{S_{25}} & \boldsymbol{S_{26}} \\ & & \boldsymbol{S_{33}} & \boldsymbol{S_{34}} & \boldsymbol{S_{35}} & \boldsymbol{S_{36}} \\ & & & \boldsymbol{S_{44}} & \boldsymbol{S_{45}} & \boldsymbol{S_{46}} \\ & & & & \boldsymbol{S_{55}} & \boldsymbol{S_{56}} \\ & & & & & \boldsymbol{S_{66}} \end{bmatrix} \begin{bmatrix} \boldsymbol{\sigma_1} \\ \boldsymbol{\sigma_2} \\ \boldsymbol{\sigma_3} \\ \boldsymbol{\sigma_4} \\ \boldsymbol{\sigma_5} \\ \boldsymbol{\sigma_6} \end{bmatrix} \quad \textbf{II.2}$$

II.3.1.3 Bulk and shear modulus:

Using the external package Thermo-pw, the elastic constants C_{ij} and the components of the compliance tensor S_{ij} were computed. Equation (II.3) and (II.4) illustrate how the polycrystalline corresponding bulk modulus (K or β) and shear modulus (G) are estimated from the computed C_{ij} and S_{ij} using the Voigt-Reuss-Hill (VRH) approximation. The subscripts R and V in these equations stand for the Reuss and Voigt bounds, respectively [31]:

- ✓ $Kr=\frac{1}{S11+S22+S33+2(S12+S23+S31)}$
- ✓ $Kv=\frac{C11+C22+C33+2(C12+C23+C32)}{9}$
- ✓ $K_{HILL}=\frac{Kr+Kv}{2}$ **II.3**

- ✓ $Gr=\frac{15}{4(S11+S22+S33)-4(S12+S23+S32)+3(S44+S55+S66)}$
- ✓ $Gv=\frac{C11+C22+C33-(C12+C23+C31)+3(C44+C55+C66)}{15}$
- ✓ $G_{HILL}=\frac{Gr+Gv}{2}$ **II.4**

II.3.1.4 Young's modulus:

The stiffness or resistance of a solid to elastic deformation under load is expressed as (*E* or *Y*). It connects strain, or proportionate deformation, along an axis o line to stress, or force per unit area. The fundamental idea is that when a material is stretched or compressed, it experiences elastic deformation, which causes it to return to its original shape when the stress is released. In comparison to a rigid substance, a flexible material deforms more. Stated differently:

- A solid is considered elastic if its young's modulus value is low.
- A solid that has a high young's modulus is stiff or inelastic [32].

The Young's modulus, E, for an isotropic material can be then estimated by [31]:

$$E=\frac{9KG}{3K+G} \quad \textbf{II.5}$$

II.3.1.5 Poisson's ratio:

Poisson's ration (symbol γ or nu) is the deformation of a material perpendicular to the loading direction. It is the negative ratio of transverse strain to axial strain [33].

It can be expressed as:

$$\gamma = \frac{3k-2G}{6K+2G} \qquad \text{II.6}$$

II.3.1.6 The elastic constants of C_{11} for MXenes:

DFT calculations have shown in great detail how the structural and mechanical properties of MXenes are significantly impacted by the functional terminations (–O, –F, –OH) of carbides. The fluctuation of the M_2CT_2 MXenes computed elastic constants C_{11} as a function of layer thickness and various functional terminations is displayed in (Figure II.8). It is evident that MXenes with oxygen functionalization had larger elastic constants than those with hydroxyl and flouring functional groups, with the exception of Cr_2CO_2 the greater contact between the oxygen and surface M is the cause of this [34].

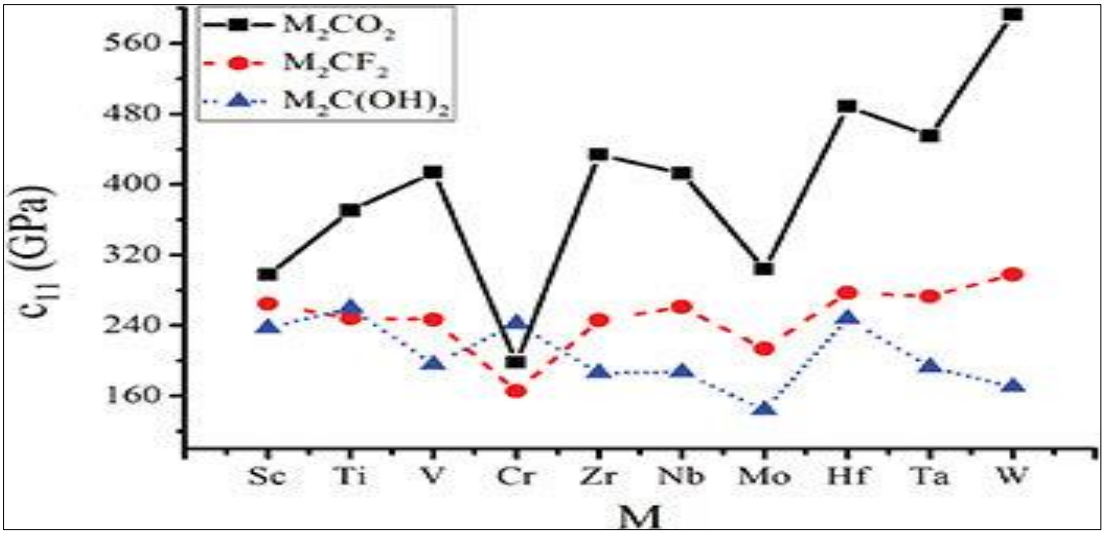


Figure II-8: The elastic constants of c11 for M_2CT_2 MXenes [34].

II.3.1.7 Elastic stability conditions:

In order to adequately characterize the mechanical properties of materials, elastic constants are crucial numbers. Clearly they are used directly at assess elastic strains or energy in materials under stress from a variety of sources, such as internal, external, thermal, etc. the shear moduli along the slip planes of mobile dislocations are strongly related to the plastic properties of materials because these dislocations can slip into partials with a spacing

dictated by the balance between the repulsive elastic force and the planar fault energy. Elastic constant values give important insights on the bonding characteristic between neighboring atomic planes, the anisotropic nature of the bonding, and structural stability. Elastic properties are also closely associated with many fundamental solid-state properties, such as acoustic velocity, thermal conductivity, interatomic potential, and so on [35].

- **Elastic constant for Rhombohedral classes:**

Uses of the symmetry simplify the number of C_{ij} depending on type of crystal type. Hence crystals in the rhombohedral I class (Laue class 3m) feature 6 independent elastic constants (see Table II-1) [36]:

$$C_{HEXA}=\begin{pmatrix} C_{11} & C_{12} & C_{13} & C_{14} & & \\ & C_{11} & C_{13} & -C_{14} & & \\ & & C_{33} & & & \\ & & & C_{44} & & \\ & & & & C_{44} & C_{14} \\ & & & & & C_{66} \end{pmatrix}$$

As in the instance of the hexagon:

$$C_{66}=(C_{11}-C_{12})/2$$

The four necessary and sufficient conditions that follow are thus obtained:

$$\begin{cases} C_{11}>|C_{12}|;\ C_{44}>0 \\ C_{13}^2<\frac{1}{2}C_{33}\,(C_{11}+C_{12}) \\ C_{14}^2<\frac{1}{2}C_{44}(C_{11}-C_{12})=C_{44}C_{66} \end{cases}$$

II.4 Other properties:

II.4.1 Magnetic properties:

Functionalized Cr2C and Cr2N MXenes (F, O, H, Cl and OH) are showing to be magnetic, although some of them show ferromagnetic-to-antiferromagnetic (FM–AFM) transitions. The d-orbitals of the Cr atoms are the source of these MXenes' magnetic properties. Given the significant energy gap that exists between Cr based MXenes' FM and AFM forms, it is possible that these systems will retain their magnetic properties almost as room temperature. According to Xiantao et al [37]. Non-terminated Cr_2C has a 2.85eV half-

metallic gap and can be ferromagnetic. The functionalization of Cr_2N MXenes with F and OH is also indicated to show antiferromagnetic properties.

II.4.2 Optical properties:

The photoluminescence (PL) emission of MADs is stronger. Owing to these properties, MXenes find widespread fields in photo-catalysis, bio sensing, photo-thermal therapy (PPT), photodynamic treatment (PDT), photo-acoustic imaging, and controlled drug release [38].

II.4.3 Conclusion:

The chapter on structural and mechanical (elastic) properties of MXenes provides a comprehensive understanding of these advanced materials. It highlights their unique structural characteristics, such as layered structure and tunable compositions, which contribute to their exceptional mechanical properties. Additional, the discussion on elastic properties underscores MXenes' ability to withstand stress and strain effectively, making them promising for various applications, including energy storage, catalysis, and electronics. Overall, the chapter illuminates MXenes as versatile materials with remarkable structural and mechanical attributes, poised to impact diverse fields of science and technology.

CHAPTER III

MXENES SURFACE TERMINATION AND THEIR EFFECTS

III MXENES SURFACE TERMINATION AND THEIR EFFECTS

III.1 Introduction:

MXenes are produced by selectively etching off the A-layer (such as Al, Si, S) of a variety of parent MAX phases. The standard formula of these etched MXenes is $M_{n+1}X_nTx$ (n = 1 to 4), where M is an early transition metal (like Ti, V, Nb, Mo), X can be either C or N, and Tx is a terminal group (e.g., –OH, –O–, –F, –Cl, –Br).

An important factor influencing the terminal group distribution of MXenes is the synthesis method. The parent MAX phase's 1-layer was etched away using intense HF in the original acid etching procedure. As a result, the produced MXenes have terminal groups with the functional groups F, OH, and O. similar to this, an in situ HF approach produces a mixture of –F, Cl, OH, and –O terminal groups by using a LiF/HCl solution as an etchant.

In 2020, Swarnima et al [39]. Developed an HF-free chemical approach for predominantly -Cl and predominantly –Br terminated MXenes, avoiding acid etching hazards and improving terminal group distribution.

III.2 Surface terminating groups of MXenes:

The -O, -OH, and –F surface terminations that are attached to the surface metal atoms of MXenes are well known to be left behind by typical etching of MXenes made using HF or HCl/LiF as etchant, as shown in Figure III-1 [40]. Surface adsorption occurs at the active sites and 2D network structure of MXenes. It is feasible to optimize the significant chemical and physical properties based on electrostatic interaction by changing the surface termination of MXenes [41].

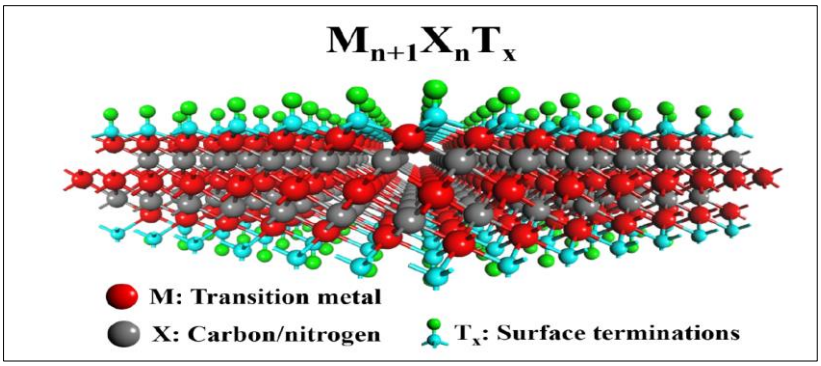


Figure III-1: Schematic illustration of the $M_{n+1}X_nTx$ MXene structures, where M is an early transition metal, X is carbon and/or nitrogen, and Tx represents surface terminations of the outer metal layers [40].

The various strategies' introduced sorts of terminations are enumerated in Table III-1. Additionally, a summary of each strategy's advantages and disadvantages is provided.

Table III-1: Comparison of the advantages and disadvantages of various synthesis strategies.

Strategies	*Terminations*	*Advantages*	*Disadvantages*
HF-based etching	_F, _OH, _O, _Cl	High efficiency Universal	-Toxic - Eco-unfriendly
Molten salt etching synthesis (> 600 _C)	_Cl, _Br or _I	Nearly single termination	High-temperature synthesis
Alkali-based etching	_OH, _O	Non-toxic	- Low efficiency - High-temperature - High-pressure synthesis
Electrochemically Assisted etching	_Cl, _O	Non-toxic	- Low efficiency - Over-etching

It is challenging to accurately control terminations or to identify their influence due to the complexity of terminations with diverse species and variable compositions. One dependable way to rapidly comprehend the structure and performance effects of terminations is, alternatively, through first-principles calculations. These potential surface locations to bridge the terminations, using M_2XT_2 as an example, are displayed in Figure III-2.

- **Model 1:** The two M atoms that are designated as "M-top" have two terminations right on top of them.
- **Model 2:** two terminations that are designated as "M-hollow" are situated on the hollow position among three nearby M atoms that face the M atom in the lattice.
- **Model 3:** the lattice "X-hollow" terminations are situated between three nearby M atoms on the hollow position, directly in front of the X atom.

By calculating the formation energies, Zhuoheng et al [42]. Suggested that, in the majority of MXenes, model 2 should be the most stable structure.

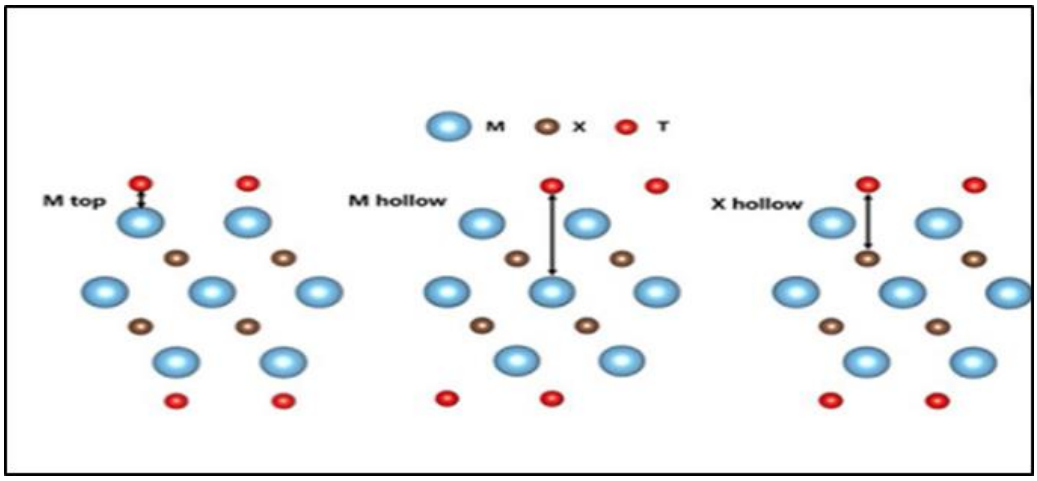


Figure III-2: Possible models for M_2XT_2 systems [42].

III.3 Stability and surface groups of MXenes:

The synthesis pathway, or more specifically, the etching reagent utilized, largely determines the kind of surface groups. –F groups are more likely to be substituted by –OH groups when stored in water, making –F terminated MXene. Groups that are –OH can change to –O groups due to metal adsorption or high temperatures. Subsequent research showed that –O group terminated (functional) MXenes can be further broken down into bare (pristine) MXenes by metal contact, such as that Mg, Ca, and Al. in most circumstances, bare MXenes are said to be reactive. When exposed to oxygen and water, bare MXenes are easily oxidized. It has also been noted that exposure to light might hasten oxidation. Thus, it is generally advised to store bare MXenes in a dry, dark, and oxygen-free environment. In most applications, surface groups functionalize MXenes because of their volatility.

The majority of the time, MXene structures are oversimplified as homogenous ending species, which does not correspond to the actual circumstances. Consequently, alternative, more accurate models must be developed to capture this intricate system since multiple surface groups may coexist and random adsorption frequently occurs simultaneously. Furthermore, it has been revealed that multilayers stacking occurs in practice, which emphasizes the significance of examining interlayer interactions such as hydrogen bonding and van der Waals forces.

Furthermore, MXenes' surface groups affect almost every other properties, including their electrical, mechanical, and optical qualities, in addition to their stability [43].

III.4 Effects of surface modification on MXene properties:

Due to the negative electric terminal groups (-F, -OH) that impede electrolyte ion transport and slow down the diffusion dynamics of Li+ and Na+, MXenes' poor compatibility with hydrophobic polymers results in low interface binding strength and poor mechanical properties. These factors significantly reduce the battery' capacity for electrical energy storage. Therefore, it is crucial to modify MXene's surface in order to alter its properties and regulate the interface.

- ✓ Friction and adhesion qualities are related to features of the MXene surface. MXene has greater adhesion and improved hydrophilicity when its friction factors are negative. The hydrophilicity of the MXene surface may lead to an increase in the interplay between strength and friction.
- ✓ The electrical structure and functionality of MXene are impacted by variations in the electrostatic potential surrounding the material's surface. The work function and the density of state can be significantly impacted by the surface groups.
- ✓ Alkyl phosphoric acid ligands were added to the acidic aqueous phase through interfacial nucleophilic addition and successive condensation processes, creating a Ti-O-P bond that was grafted to the MXene surface. The solubility of MXene in nonpolar organic solvents is increased by depending on the solvation effects of strong nonpolar effects and the spatial stability of long alkyl chains [44].

III.4.1 Influence of terminations on mechanical properties:

MXenes' surface terminations are thought to be a major contributor to their mechanical properties. When compared to –OH and –F terminated MXenes, O-terminated MXenes often exhibit greater stiffness [45]. Put succinctly, M_2CO_2 MXenes typically exhibit lower lattice parameters and layer thicknesses than M2CT2 (T=-F, -OH) members. Further resulting in reduced volumes are the layer thicknesses and lattice parameter reductions. Notably, it has been discovered that the oxygen-functionalized MXenes' larger volume capacity and smaller molar volumes may help them work better in super-capacitors. When compared to equivalent MXenes functionalized by fluorine and hydroxyl groups, the oxygen-functionalized MXenes aside from Cr_2CO_2 present greater elastic constants. [46]

The different terminal groups are responsible for this, phenomenon. For instance, Mozafari et al [45]. Found that the surface functionalization of Ti_3C results in a drop in young's modulus but an increase in strain and flexibility. The various functional groups on the surface

of MXenes operate as a delimiter under tensile deformation, increasing the critical strain and slowing down the collapse of Ti layers. The number of atomic layers of MXenes, according to their chemical formula, is another aspect that affects their mechanical properties. Accordingly, other researchers, discovered that as n decreases, so do the hardness and tensile strength of a $M_{n+1}X_n$ MXene. Moreover, adding CNTs and polymerizing with different kinds of polymers might 3 the mechanical qualities of MXenes. In comparison to pure MXenes, composites exhibit greater toughness, flexibility and tensile strengths. When compared to pure Ti_3C_2, the Ti_3C_2/PVA composite, for example, showed a higher tensile strength. Furthermore, the yield strength and toughness of Ti3C2/polyacrylamide (PAM) and Ti_3C_2/ ultrahigh molecular weight polyethylene (UHMWPE) composites are higher than those of pure Ti_3C_2.

III.5 Conclusion:

In conclusion, the surface termination of MXenes is a critical aspect that significantly influences their properties and potential applications it can also affect their stability, conductivity, and even their interaction with other materials. The outlook for surface termination of MXenes is quite promising, researchers are actively exploring different surface termination to unlock new properties and application. By tailoring the surface termination, we can enhance the stability, conductivity, and reactivity of MXenes, making them more versatile for various fields.

Further research into understanding and controlling surface termination will be essential for unlocking the full potential of MXenes in various fields ranging from energy storage to catalysis, and beyond.

COMPUTING PART

CHAPTER IV

STUDY OF THE EFFECT OF SURFACE TERMINATION ON THE PROPERTIES OF MXENES Cr_2CT_2 MATERIAL (CASE OF T=OH AND O GROUPS)

IV STUDY OF THE GEOMETRIC AND ELASTIC PROPERTIES OF Cr_2CO_2 AND $Cr_2C(OH)_2$ MXENES.

IV.1 Introduction:

In this chapter, we will study and interpret the results obtained from the CASTEP module included in the software MATERIALS STUDIO (2024 version). The study delves into the intricate relationship between terminal groups and the structural, as well as mechanical (elastic) properties of Cr_2CT_2 MXene. Specifically, it investigates the influence of T=OH ($Cr_2C(OH)_2$) and T=O (Cr_2CO_2) groups on these properties.

BIOVIA MATERIALS STUDIO (MS) is a simulation environment designed to allow and help chemistry and materials science researchers forecast and comprehend how a material's atomic and molecular structure relates to its properties and behavior [47], MS integrates many modules that cater to different aspects of materials research such as CASTEP.

A quantum mechanics-based program made especially for solid-state materials science is called CASTEP (Cambridge serial total energy package). With the aid of CASTEP, one can examine the properties of crystals and surfaces in materials through first-principles quantum mechanics calculations using the plane-wave pseudo-potential approach of density functional theory (DFT) [48]. In CASTEP GGA and PBE are most commonly used density functional for performing structure calculations.

DFT is a series of approaches for electronic structure computations in quantum mechanics that find wide applications in main groups and organic compounds as well as more complex systems. These techniques are especially useful for complexes of transition metals, where there may be significant electron correlation effects [49]. We are using strong computational techniques to delve deeply into the details of our MXenes by applying DFT.

This work aims to applying pressure to explore the structural geometry and elastic properties of $Cr_2C(OH)_2$ and Cr_2CO_2 which is crucial for understanding their mechanical (elastic) behavior. By subjecting these compounds to varying pressure conditions, we can observe changes in their crystal structures, such as phase transitions or lattice distortions. Furthermore, investigation of the elastic properties under pressure can provide insights into their deformation mechanisms and potentials for applications in areas such as high-pressure manufacturing processes or structural materials for extreme environments.

IV.2 Description of the crystal structure of the MXene Cr_2CO_2 and $Cr_2C(OH)_2$ phase material:

The crystal structure of MXene materials Cr_2CO_2 and $Cr_2C(OH)_2$ is typically layered. In these structures, transition metal (M) atoms, such as chromium (Cr), form layers with carbon (C) atoms sandwiched between them. The layers are held together by a strong bonds.

With the matching M_2CF_2 members, other M_2CO_2 MXenes exhibit comparable layer thicknesses [46]. (MXenes like, $Cr_2C(OH)_2$, Cr_2CH_2 and Cr_2CCl_2, show similar lattice structure as Cr_2CF [50]).

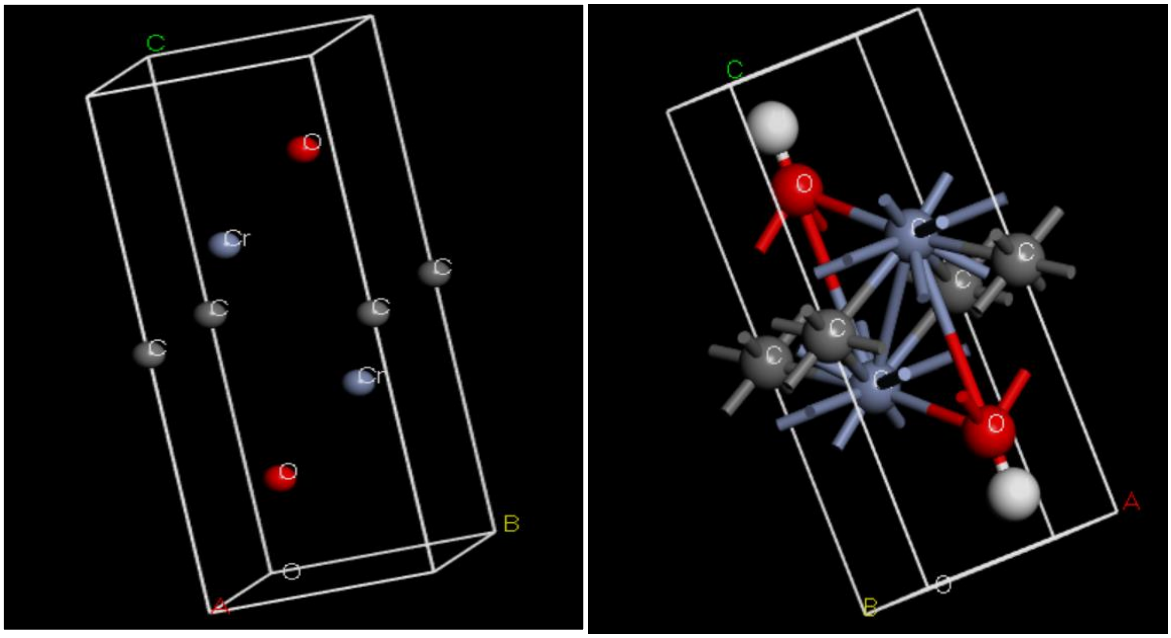
The Cr_2CO_2 and $Cr_2C(OH)_2$ MXene has an important metallic and ceramic properties, in the case of our study we will consider them as a metal in CASTEP. We use the elemental crystal TRIGONAL system lattice of hexagonal symmetry, belonging to the group space 164, this symmetry is characterized by a hexagonal unit cell with threefold rotational symmetry along the c-axis and mirror symmetry in the basal plane (P-3m1) as illustrated in FigureIV-1.

After persistent efforts, successfully obtaining a stable and optimized geometry along with new lattice parameters for the compounds Cr_2CO_2 and $Cr_2C(OH)_2$ (see Table IV-1).

Table IV-1: The lattice parameters of Cr_2CO_2 and $Cr_2C(OH)_2$ MXenes.

MXenes / **Lattice parameters**	**a (A°)**	**b (A°)**	**c (A°)**	**α=β**	**γ**
Cr_2CO_2	2.774362	2.774362	7.121051	90°	120°
$Cr_2C(OH)_2$	3.036635	3.036635	7.888366	90°	120°

(a) **(b)**



FigureIV-1: (a) crystal structure of Cr_2CO_2, **(b)** $Cr_2C(OH)_2$ established by geometric optimization.

We save and upload the optimized geometric of Cr_2CO_2 and $Cr_2C(OH)_2$ to MATERIAL STUDIO program, according to the steps which are shown in the following figures.(Figure IV-2, Figure IV-3, Figure IV-4).

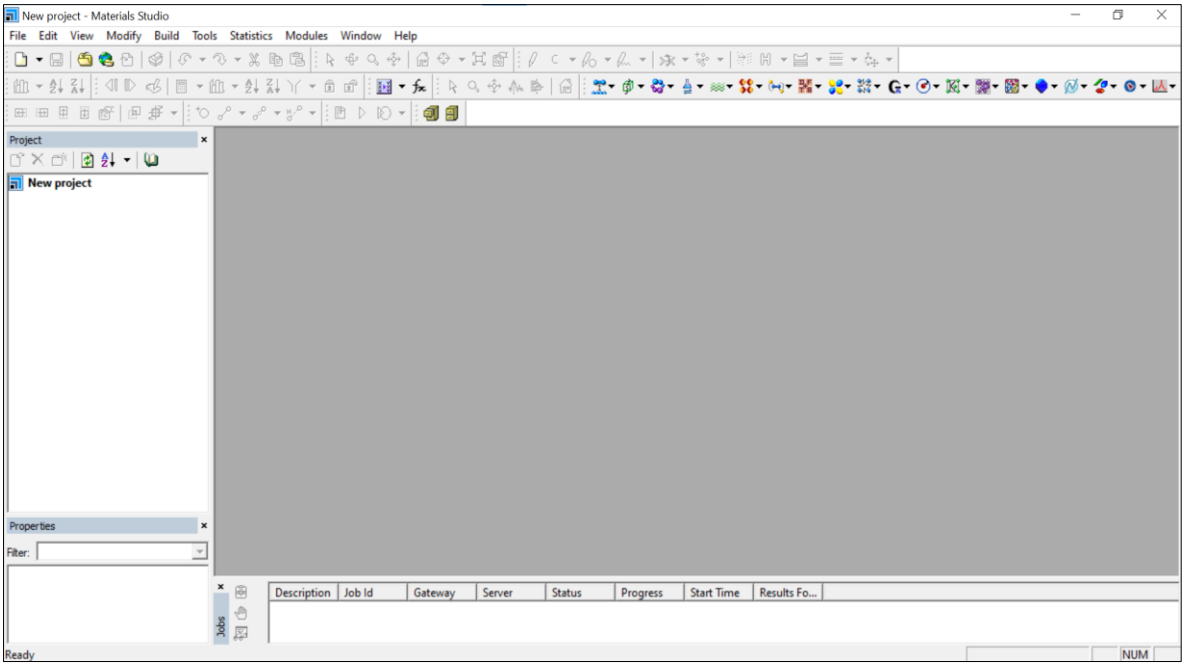


Figure IV-2: Open the MATERIAL STUDIO program.

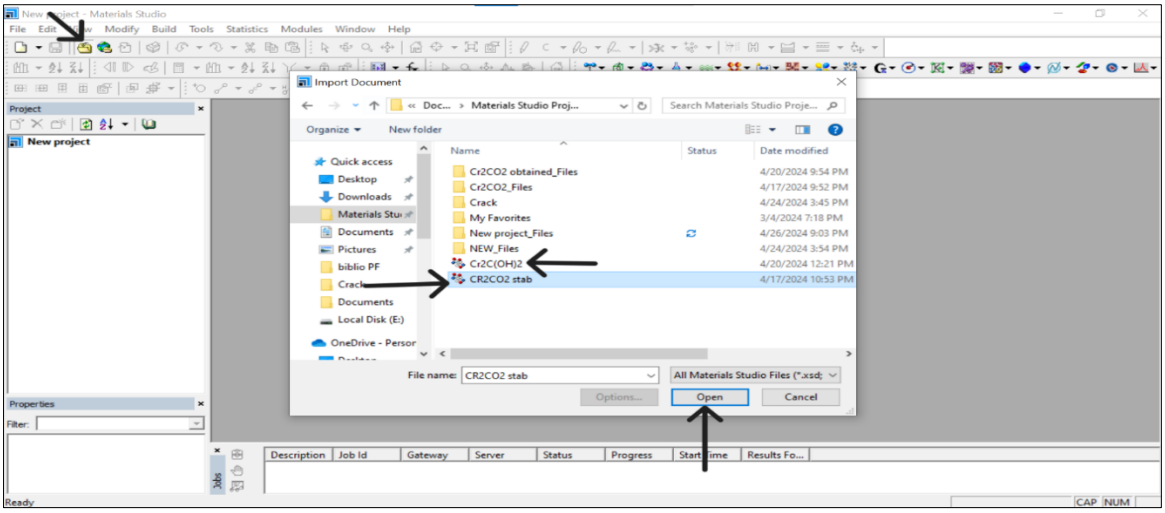


Figure IV-3: Choose the import icon, then open the geometric file respectively.

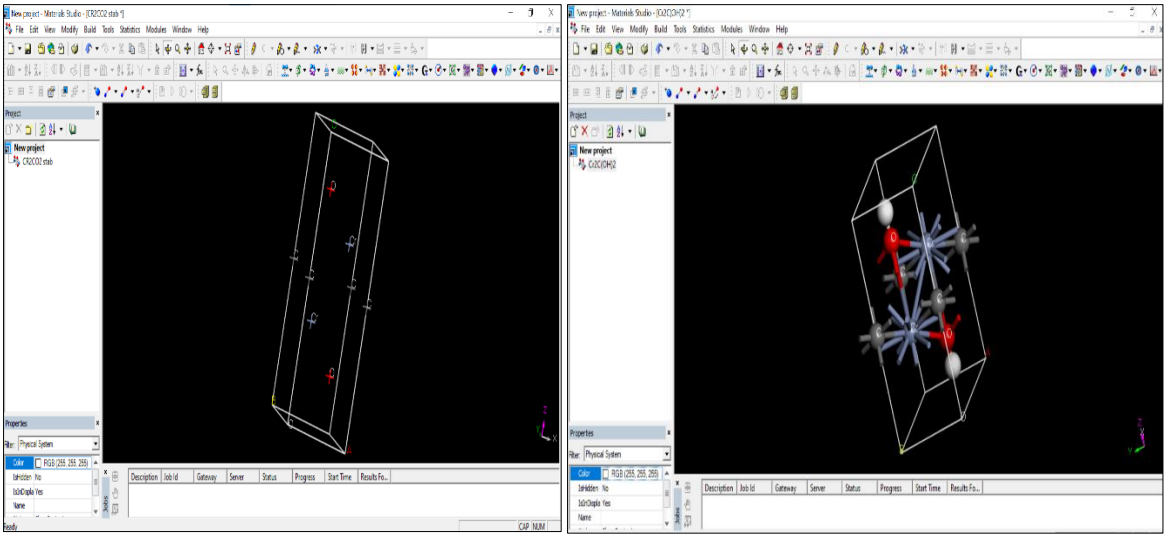


Figure IV-4: Open files in the program appear as follows.

MATERIAL STUDIO's capabilities extend beyond mere geometric visualization, encompassing features that cater to intricate structural analysis. Which it's also adept at handling with the symmetry of the structures that we need in our study through the following steps:

- Build
- Symmetry
- Show symmetry and find symmetry

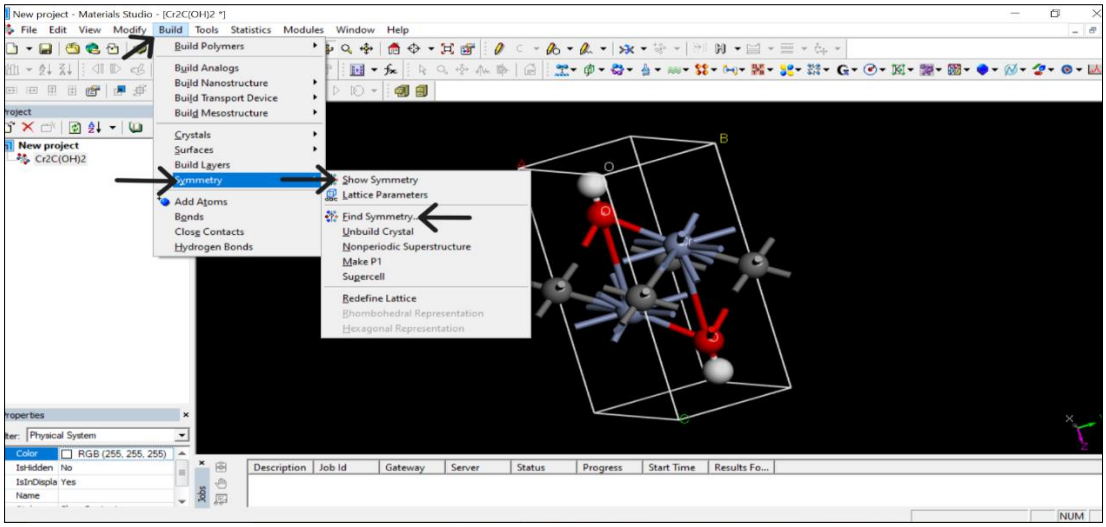
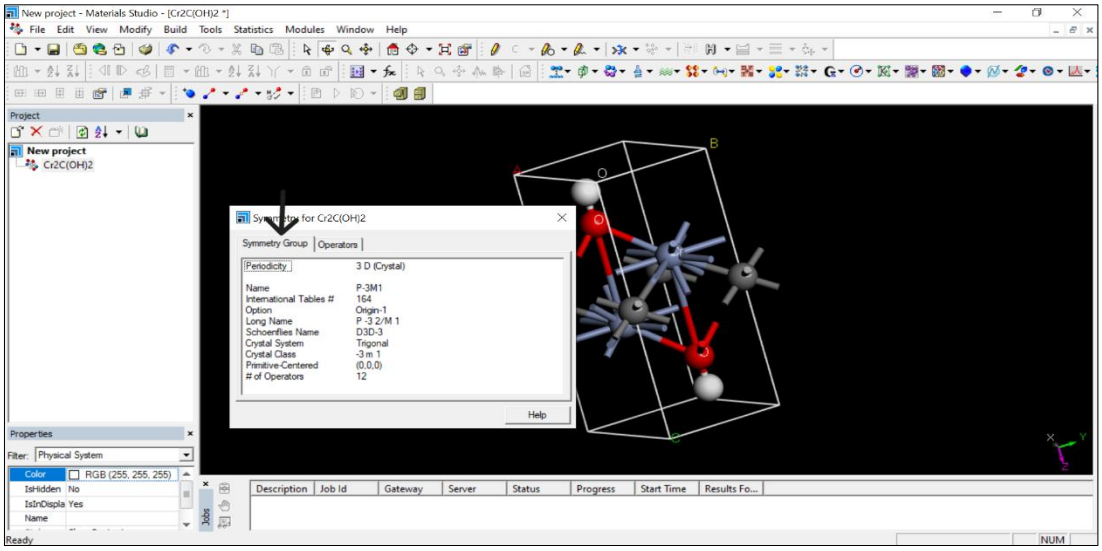
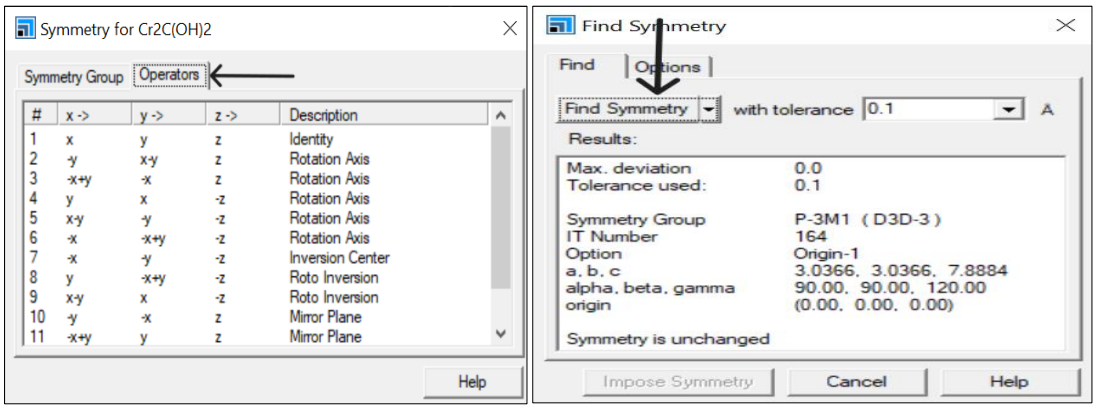


Figure IV-5: show symmetry parameter.

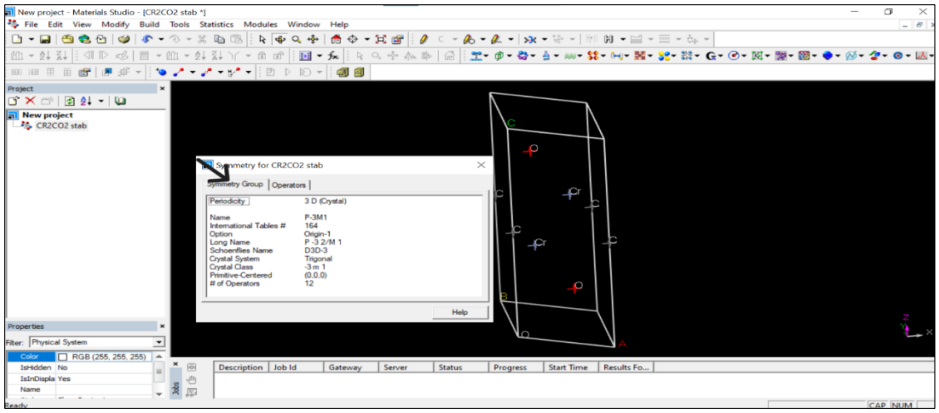
(a)



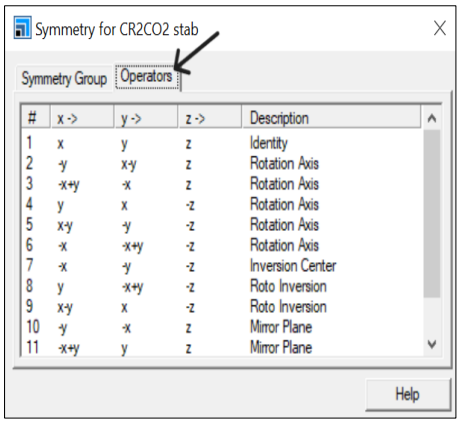


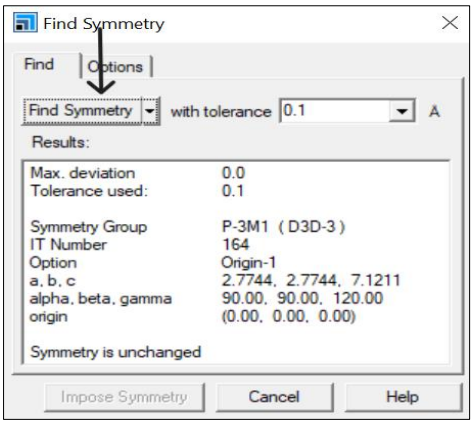
(b) **(c)**

Figure IV-6: **(a)**: show the symmetry group, **(b)**: Operators symmetry, **(c)**: and the symmetry of $Cr_2C(OH)_2$ MXene.



(a)





(b) **(c)**

Figure IV-7: **(a)**: show the symmetry group, **(b)**: Operators symmetry, **(c)**: and the symmetry of Cr_2CO_2 MXene.

IV.3 Geometric optimization of the structures:

In the optimization process within CASTEP in MATERIALS STUDIO, adjusting the pressure serves as a crucial step in understand the deformation response to external loads and consequently making/choosing the desired material structure.

In this phase, before commencing, it's imperative to meticulously adjust a multitude of parameters to ensure the ideal setup. The pressure exerted on the structure induces volumetric deformations, compression, elongation, and shearing highlighting the need to ascertain to optimal geometric form through total energy minimization. In MATERIALS STUDIO, this process unfolds as follows:

- Select the CASTEP code.
- Calculations.

We adjust the geometric optimization parameters using the GGA-PBESOL exchange and correlation functional for both Cr_2CO_2 and $Cr_2C(OH)$. While also factoring in the pressure applied to the structure via the super-cell representation. Upon completion of the optimization, we generate a CASTEP extension file containing the optimized lattice data (see Figure IV-8).

After making the modifications, we initiate the optimization process by selecting “Run” option (see Figure IV-9).

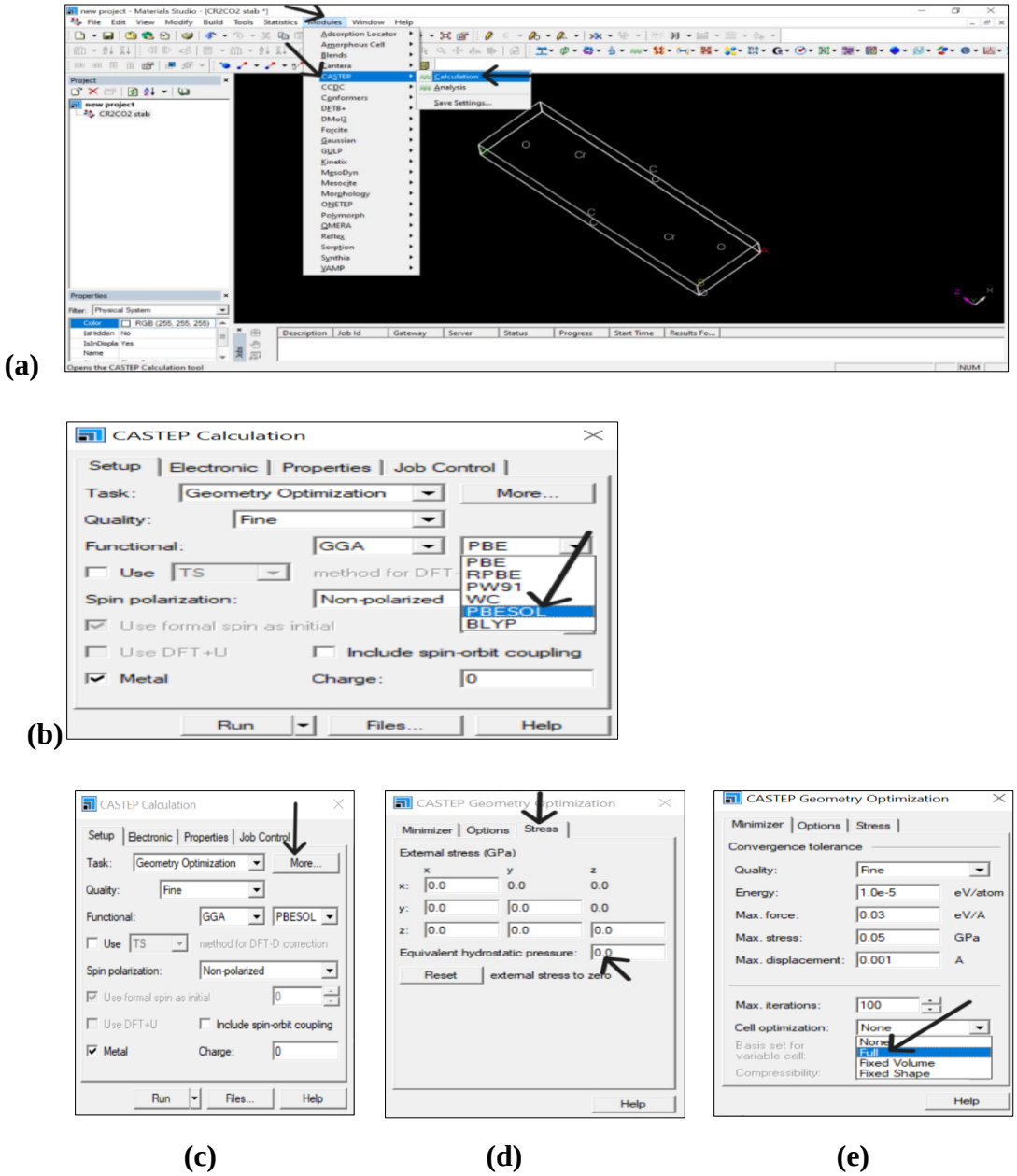


Figure IV-8: (a): Access calculations from the CASTEP model, **(b)**, **(c)**, **(d)** and **(e)** parameters modified before optimization.

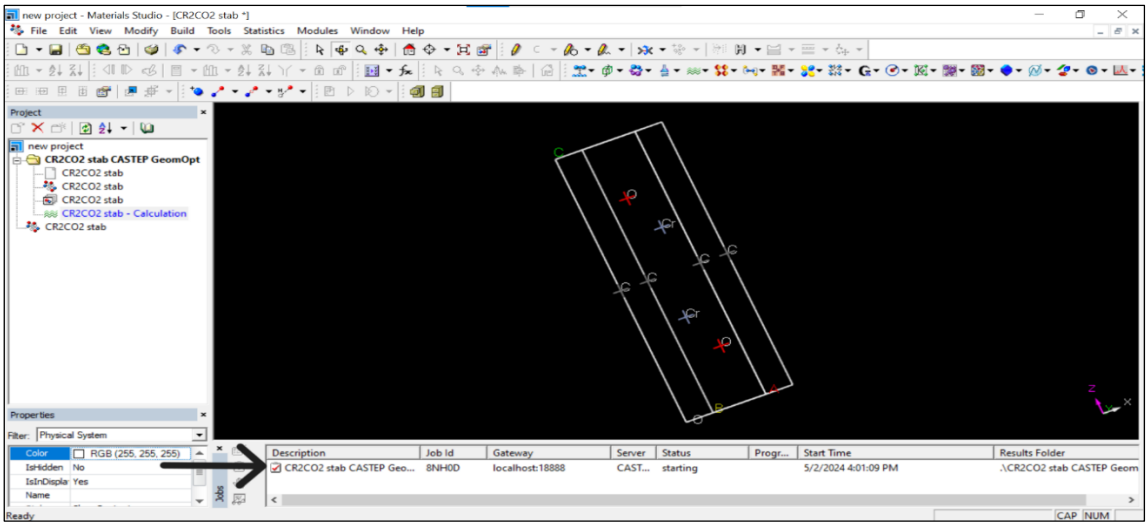


Figure IV-9: start and currently undergoing optimization.

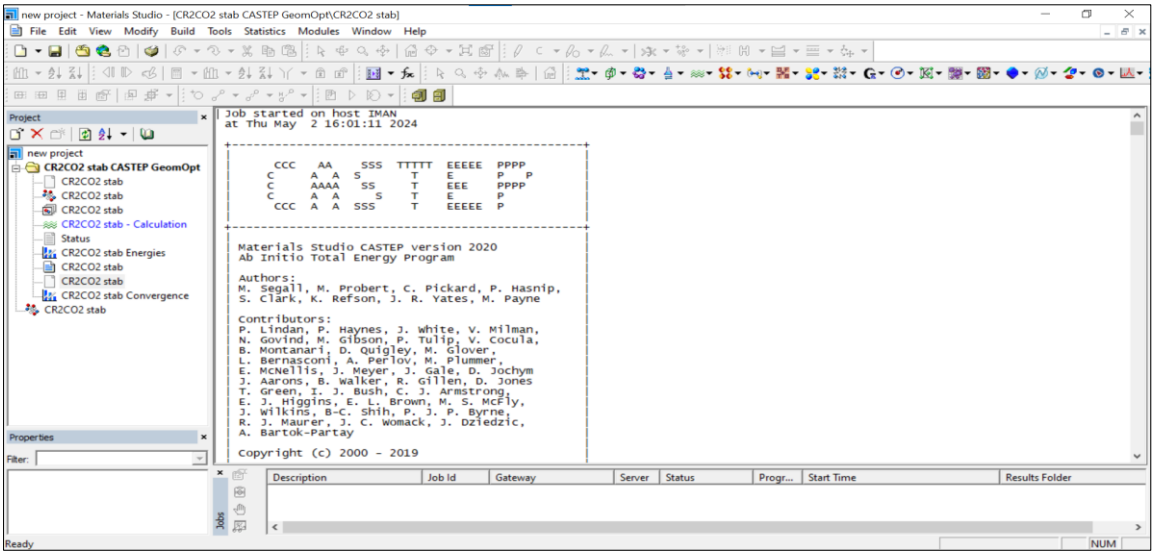
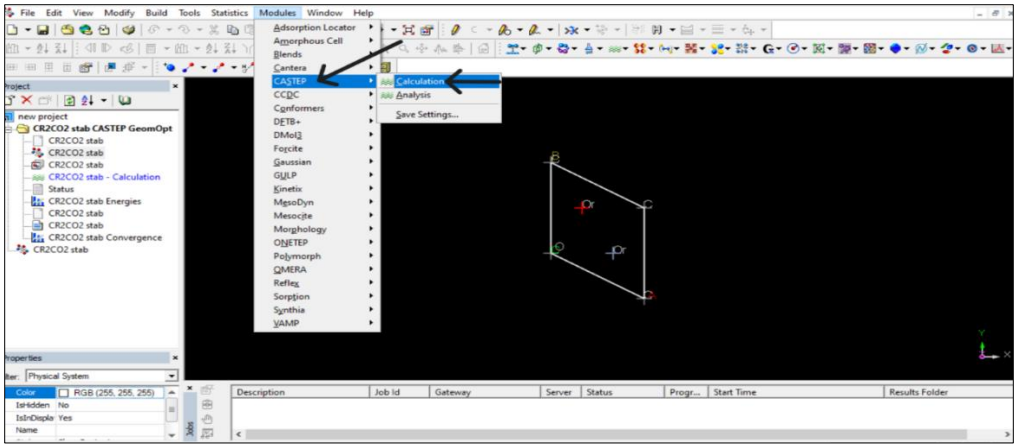


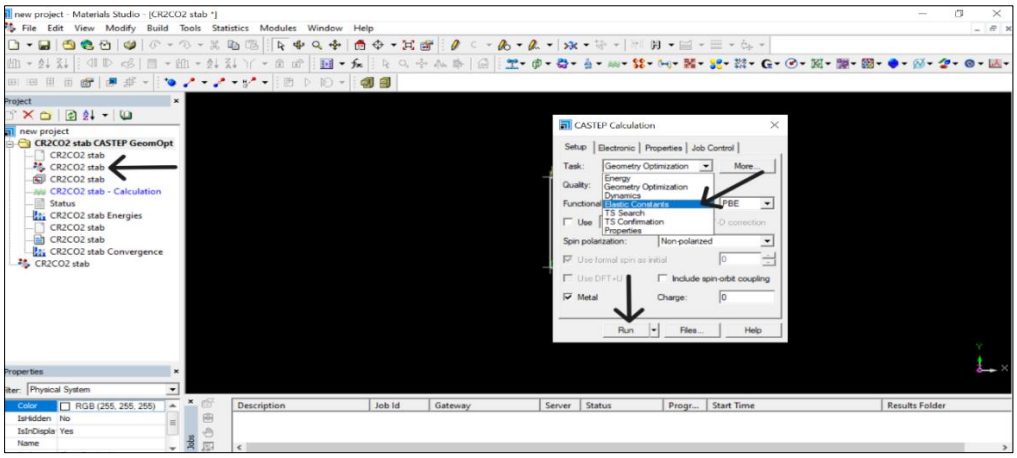
Figure IV-10: optimization completed.

IV.3.1 Computes elasticity tensors:

Now, transitioning to the subsequent phase involves computing the elastic properties. This entails repeating the earlier procedures, albeit with a focus on selecting elastic constants instead of geometric optimization, followed by click on ran (see Figure IV-11).



(a)



(b)

Figure IV-11: **(a)**: choose CASTEP then calculation. **(b)**: select the optimized geometry, choose elastic constants then press RUN.

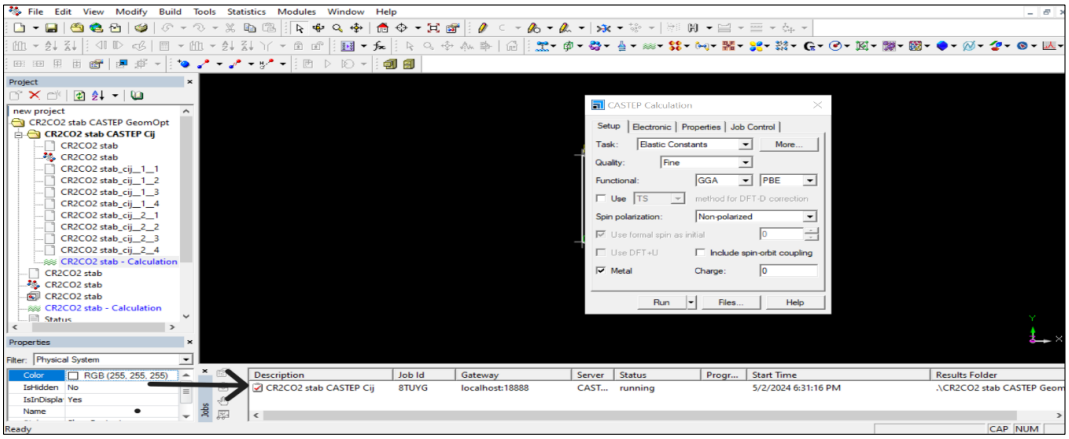


Figure IV-12: starting the calculations.

Once the program completes its calculations, we select CASTEP once more, instead of opting calculations, we navigate to the analysis section, specifically targeting elastic constants. Finally, we utilize the calculate button to display the obtained results (see Figure IV-13).

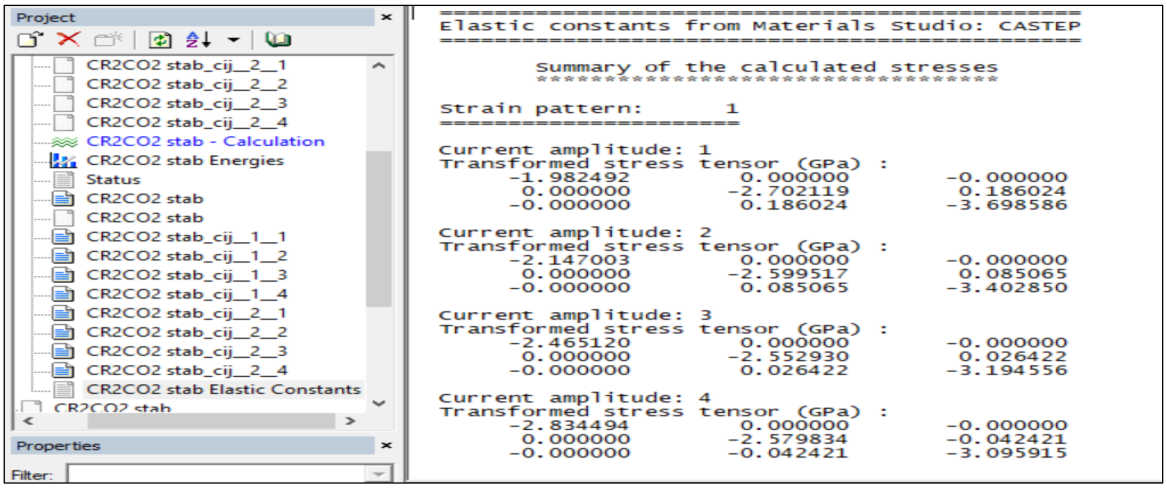


Figure IV-13: results obtained after calculation and analysis.

IV.4 Variation of structural properties:

IV.4.1 Behavior of network constants:

The lattice parameters after deformation for Cr_2CO_2 and $Cr_2C(OH)_2$ under increasing pressures are shown in (Table IV-2 and Table IV-3), following geometric optimization. To clarify further, the table date was plotted in the Figure IV-14.

Table IV-2: Evolution of the lattice parameters of the Cr_2CO_2 structure depending on the pressure.

Pressures (GPA) / ***lattice parameters***	a=b (A°)	c (A°)	a/c	v (A**3)	d (amu/A**3)
0	2.741402	7.544043	0.363386	49.09986	3.014286
10	2.706576	6.76352	0.400173	42.90855	3.449219
20	2.67741	6.591272	0.406205	40.91945	3.616886
30	2.650983	6.488157	0.408588	39.48806	3.747994
40	2.626223	6.418636	0.409156	38.33863	3.860362
50	2.603339	6.365664	0.408966	37.36248	3.96122
60	2.581806	6.324138	0.408246	36.50726	4.054015
80	2.542696	6.260889	0.406124	35.05545	4.221911
100	2.508274	6.213145	0.403704	33.8526	4.371924
200	2.379305	6.067762	0.392122	29.74812	4.975138
300	2.29309	5.969171	0.384156	27.18233	5.44475
400	2.225617	5.903196	0.377019	25.32321	5.844481
500	2.166595	5.866727	0.3693132	23.849645	6.205585
600	2.113776	5.857712	0.360854	22.666092	6.529621
700	2.065693	5.861359	0.352426	21.66011	6.832883
800	1.96586	5.803577	0.338732	19.42369	7.619614

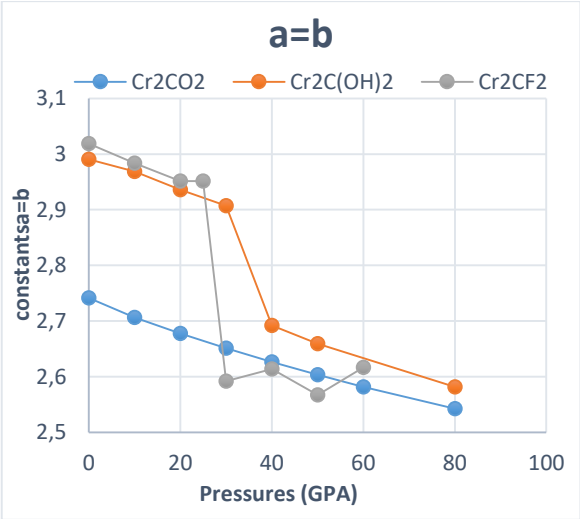
From the Table IV-2 we can see how the proportions of the unit cell change under varying pressures. As pressure increases the a/c ratio rises, indicating that the lattice parameters "a=b" are compressing less than "c" initially, the a/c ration continues to increase slightly, peaking around 40 GPA. Beyond 40 GPA the ratio starts to decrease gradually. This trend indicates that at higher pressures, the "c" parameter compresses at a slower rate compared to "a" and "b", leading to a decrease in the ratio a/c.

Table IV-3: Evolution of the lattice parameters of the $Cr_2C(OH)_2$ structure depending on the pressure.

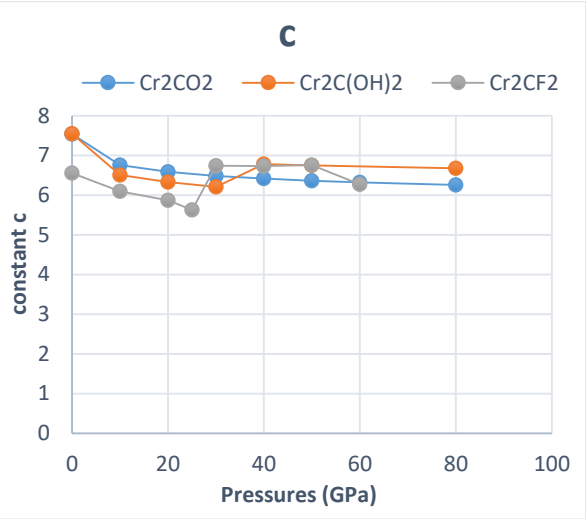
Pressure (GPA) / ***Lattice parameters***	a=b (A°)	c (A°)	a/c	v (A*3)	d (amu/A*3)
0	2.990773	7.549571	0.39615138	58.481675	2.565197
10	2.968856	6.505982	0.45632712	49.661728	3.020789
20	2.935908	6.335921	0.4633751	47.296101	3.171868
30	2.907320	6.213837	0.46787838	45.485829	3.298104
40	2.691976	6.787366	0.39661571	42.596520	3.521813
50	2.659243	6.755149	0.39366163	41.369626	3.626259
80	2.581658	6.679940	0.38647922	38.556760	3.890809

From the Table IV-3 we observe: lattice parameters "a=b" slightly decrease with increasing pressure, indicating a contraction of the lattice in these directions. Lattice parameter "c" also decreases with pressure, but not as uniformly as "a=b". The a/c ratio increases initially with pressure, showing that "a=b" contract faster than c, then it decreases again, showing a more complex relationship between the parameters under high pressure. Unite cell volume "v" decreases steadily with pressure, which is expected as the material compresses. Density "d" increases densification with pressure, reflecting the decrease in unit volume under constant mass. To farther illustration, we have reported in Figure IV-14 the behavior of unit cell under different constraints and compared them to that found in earlier study [51].

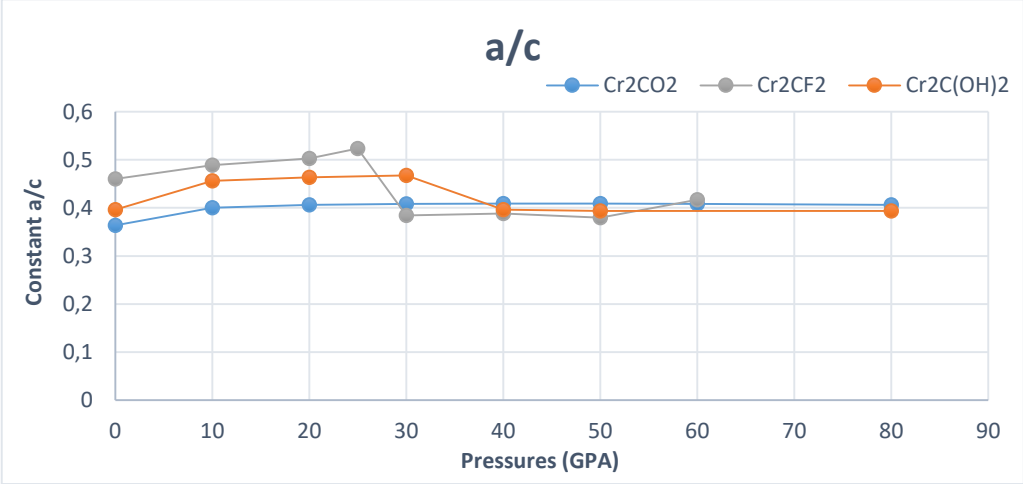
Although we observe a regular decrease in a and c parameter of Cr_2CO_2 structure when pressure increase, a slight break in a parameter is observed between 30 and 40 GPA for both


a=b
Cr2CO2
Cr2C(OH)2
Cr2CF2
constantsa=b
Pressures (GPA)

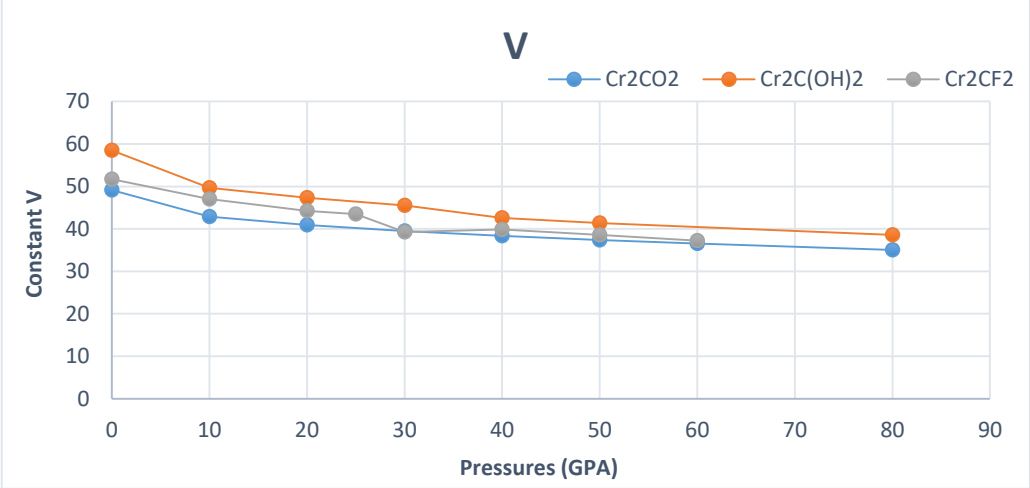
(a)


c
Cr2CO2
Cr2C(OH)2
Cr2CF2
constant c
Pressures (GPa)

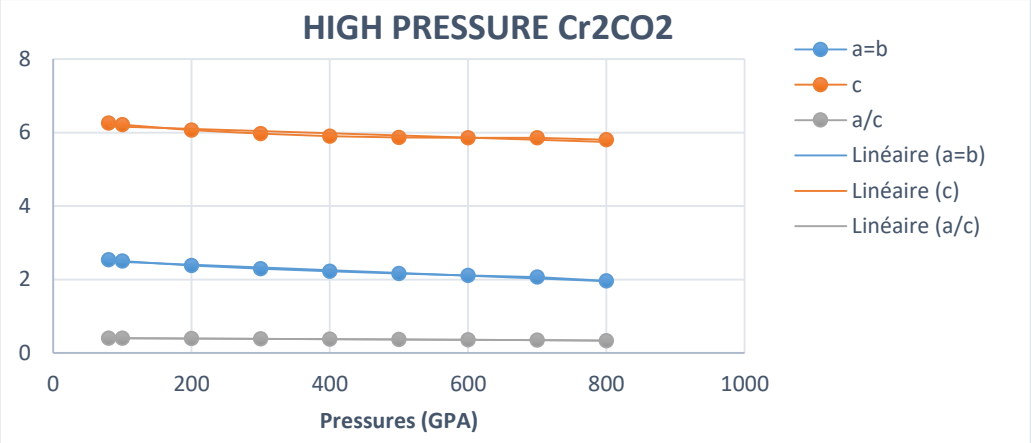
(b)


a/c
Cr2CO2
Cr2CF2
Cr2C(OH)2
Constant a/c
Pressures (GPA)

(c)


V
Cr2CO2
Cr2C(OH)2
Cr2CF2
Constant V
Pressures (GPA)

(d)



(e)

Figure IV-14: (a), **(b)**: variation of the constants "a=b" as a function of pressure, **(c)**: variation of the a/c ratio as a function of pressure, **(d)**: variation of volume as a function of pressure, for the three MXenes, **(e)**: high pressure of Cr_2CO_2 for different lattice parameters.

IV.4.2 Variations of elastic properties:

After the results obtained from the elastic calculations and analysis for the Cr_2CO_2 and $Cr_2C(OH)_2$ structures, we verify the validity of the results using the conditions that were mentioned in the second chapter, which are as follows:

- ✓ $C_{66}=(C_{11}-C_{12})/2$
- ✓ $C_{11}>|C_{12}|;\ C_{44}>0$
- ✓ $C_{13}^2 < ½C_{33}(C_{11}+C_{12})$
- ✓ $C_{14}^2 < ½C_{44}(C_{11}-C_{12}) = C_{44}C_{66}$

The following table represent an example of calculation at pressure 20 GPA.

Table IV-4: The stress tensors for (Cr_2CO_2).

C_{ij}	C_{i1}	C_{i2}	C_{i3}	C_{i4}	C_{i5}	C_{i6}
C_{1j}	416.86825	241.78260	205.28510	36.09020	0.00000	0.00000
C_{2j}	241.78260	416.86825	205.28510	-36.09020	0.00000	0.00000
C_{3j}	205.28510	205.28510	327.26940	0.00000	0.00000	0.00000
C_{4j}	36.09020	-36.09020	0.00000	53.62580	0.00000	0.00000
C_{5j}	0.00000	0.00000	0.00000	0.00000	53.62580	36.09020
C_{6j}	0.00000	0.00000	0.00000	0.00000	36.09020	87.54282

We verified the stability conditions for every constraint used for the both Cr_2CO_2 and $Cr_2C(OH)_2$ MXenes:

- **Cr_2CO_2 MXene:**

From [0 GPA to 800 GPA] is confirmed, so it's remain elastically stable.

- **$Cr_2C(OH)_2$ MXene:**

From [0 GPA to 30 GPA] is confirmed, at [30GPA] we see that the stability conditions don't verify, so there is a significant deformation, which makes the structure different from what it was originally.

IV.4.3 Study of the variation of the elasticity tensors:

In conducting a DFT—GGA analysis, we derived the numerical values for the 7 distinct elastic constants (see Table IV-5 and Table IV-6). It's important to highlight that C_{11} and C_{33} reflect the material's stiffness under a uniaxial stress along the primary directions. Additionally, C_{44} signifies the material's resistance to shear stress when applied on the plane aligned with the x-axis in the direction of y. Figure IV-15 shows the variation in elasticity tensors for Cr_2CO_2, $Cr_2C(OH)_2$, and Cr_2CF_2 as a function of pressure.

- **Cr_2CO_2 MXene:**

Table IV-5: stress tensor values (Cr_2CO_2).

Pressure (GPA) / C_{ij}	C_{11}	C_{12}	C_{13}	C_{14}	C_{33}	C_{44}	C_{66}
0	-190.175	434.066	-9.67125	5.4691	18.64345	8.0601	-312.12
10	248.4068	171.4076	59.5991	22.62325	232.5717	27.24225	38.4996
20	416.8683	241.7826	205.2851	36.0902	327.2694	53.6258	87.54282
30	482.3832	263.6173	261.0389	44.82685	432.8801	56.10525	109.383
40	536.6076	273.9775	307.1695	65.88175	489.9797	85.2441	131.3151
50	549.0427	289.5009	326.7665	71.62085	523.1508	91.16585	129.7709
60	569.5568	350.6351	380.4469	78.33655	561.7728	93.3672	109.4609
80	652.0546	396.8828	450.2725	92.147	757.8668	122.0409	127.5859
100	809.1548	446.6514	535.333	91.6177	866.7927	150.7386	181.2517
200	1260.222	711.6522	847.0499	119.0283	1474.228	285.0437	274.285
300	1567.312	966.2787	1149.531	166.6418	1930.436	374.1513	300.517
400	1856.508	1215.256	1400.435	217.7301	2387.319	462.5601	320.626
500	2099.249	1423.11020	1653.0664	299.77120	2869.015	541.7629	338.0693
600	2379.045	1755.605	2087.094	334.87775	3056.196	623.799	311.72
700	2790.056	1937.345	2242.616	369.824	3679.921	699.028	426.355
800	3513.340	2862.492	2937.4750	378.2719	4983.437	829.300	325.4241

We can see from Table IV-5 that the tensors C_{ij} have linear values that grow with pressure. The values of $C_{14}, C_{44},$ and C_{66} Increase linearly, but with a small slope compared to C_{11}, C_{12}, C_{13}, and C_{33}, it has the lowest sensitivity.

Cr_2CO_2 is characterized by a high value of C_{11}, C_{12}, C_{13}, and C_{33} compared to C_{14}, C_{44}, and C_{66}.

- ✓ **C_{11} and C_{33}:** High values indicate the material is very stiff and resistant to compressive or tensile forces along the principal axes.
- ✓ **C_{12} and C_{13}:** High values signify strong coupling between different directions of stress and strain. This implies anisotropy in mechanical properties, meaning that Cr_2CO_2 behaves differently when stressed in different directions.

➢ $Cr_2C(OH)_2$ MXene:

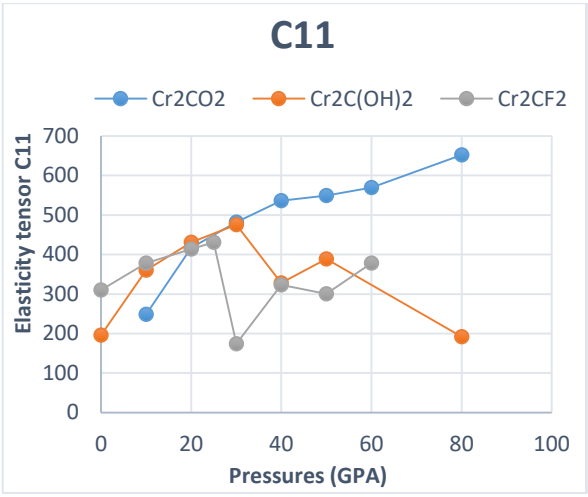
Table IV-6: stress tensor values ($Cr_2C(OH)_2$).

Pressure (GPA) / C_{ij}	C_{11}	C_{12}	C_{13}	C_{14}	C_{33}	C_{44}	C_{66}
0	196.3218	154.3228	0.94635	1.7678	-25.7204	19.1541	20.99948
10	360.8469	218.5004	83.09785	-4.59475	233.1928	57.8922	71.17327
20	430.6776	251.7517	131.583	10.863	327.7868	73.397	89.46292
30	475.4087	286.7942	160.5523	12.09555	380.2304	99.5062	94.30727
40	327.6861	351.64935	330.29255	30.85505	432.54545	128.29920	-11.98162
50	389.153	380.4466	359.8906	36.3874	547.2092	146.4657	4.35322
80	192.0416	128.4007	7.2659	0.8497	-36.72185	9.50685	31.82045

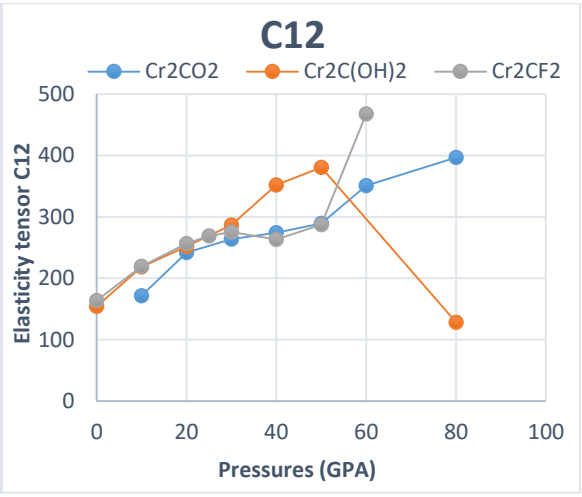
From Table IV-6 we notice that the value of the tensors C_{ij} (except for C_{14}) increase linearly as function of pressure up to the limit of the elastic domain of MXene.

The value of C_{13}, C_{44}, and C_{66} increase linearly but with low spawning compare with the other soft C_{14}, they have low sensitivity.

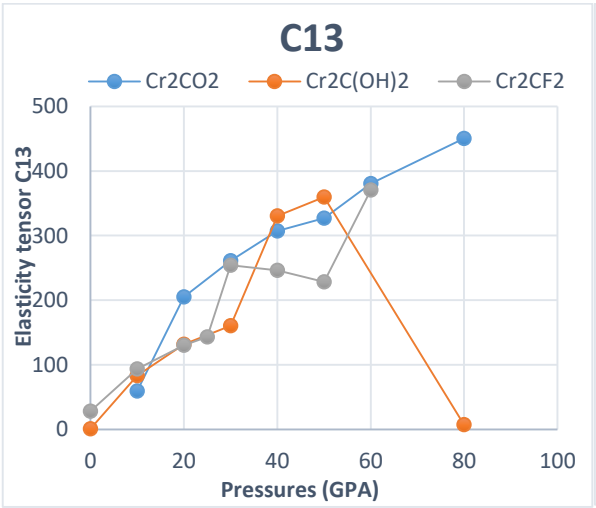
$Cr_2C(OH)_2$ is characterized by a high value of C_{11} and C_{13} compared to the other elastic tensors, which significant that is very stiff and resistant to compressive or tensile forces along the principal axes.


C11
Cr2CO2
Cr2C(OH)2
Cr2CF2
Elasticity tensor C11
Pressures (GPA)

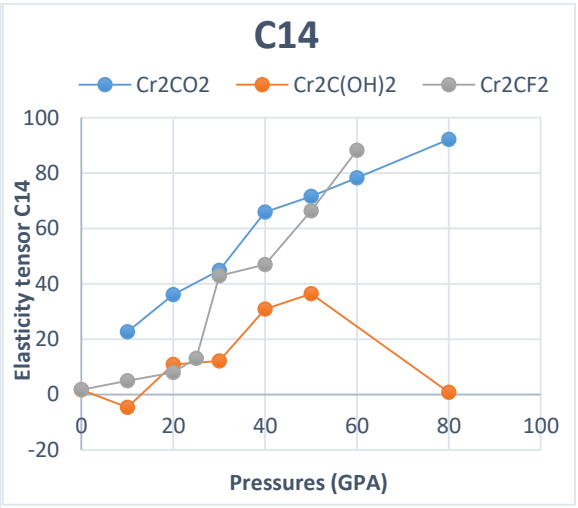
(a)


C12
Cr2CO2
Cr2C(OH)2
Cr2CF2
Elasticity tensor C12
Pressures (GPA)

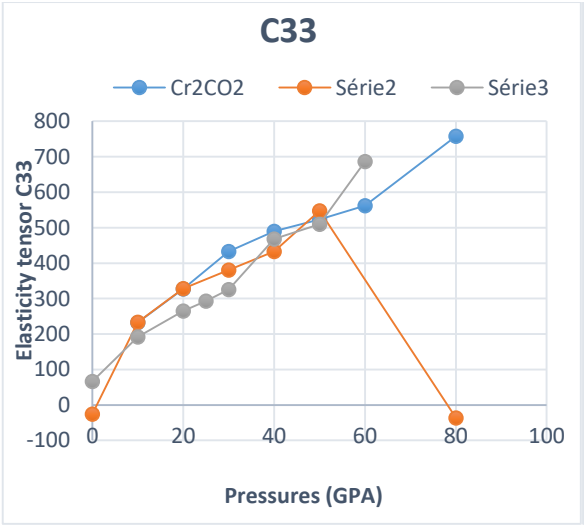
(b)


C13
Cr2CO2
Cr2C(OH)2
Cr2CF2
Elasticity tensor C13
Pressures (GPA)

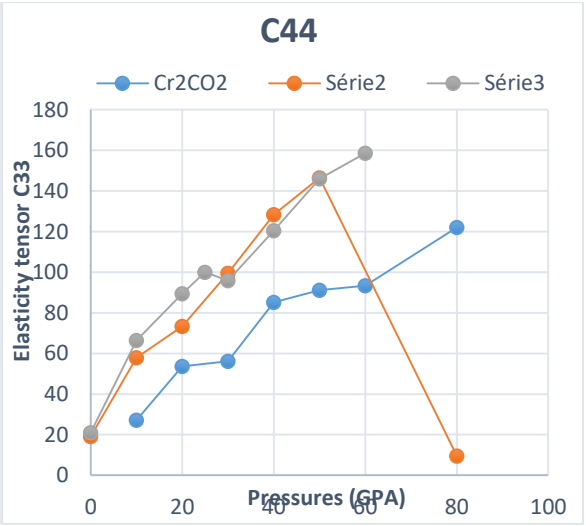
(c)


C14
Cr2CO2
Cr2C(OH)2
Cr2CF2
Elasticity tensor C14
Pressures (GPA)

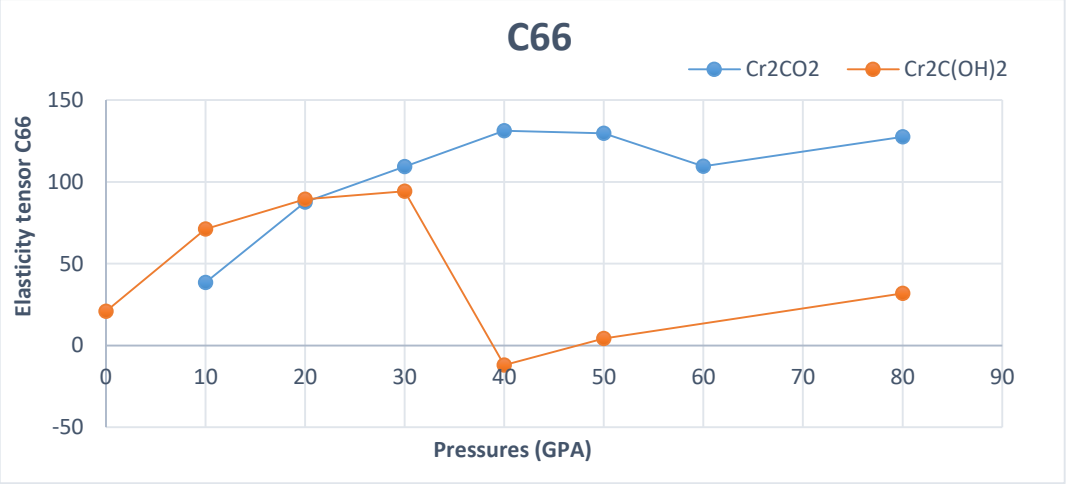
(d)


C33
Cr2CO2
Série2
Série3
Elasticity tensor C33
Pressures (GPA)

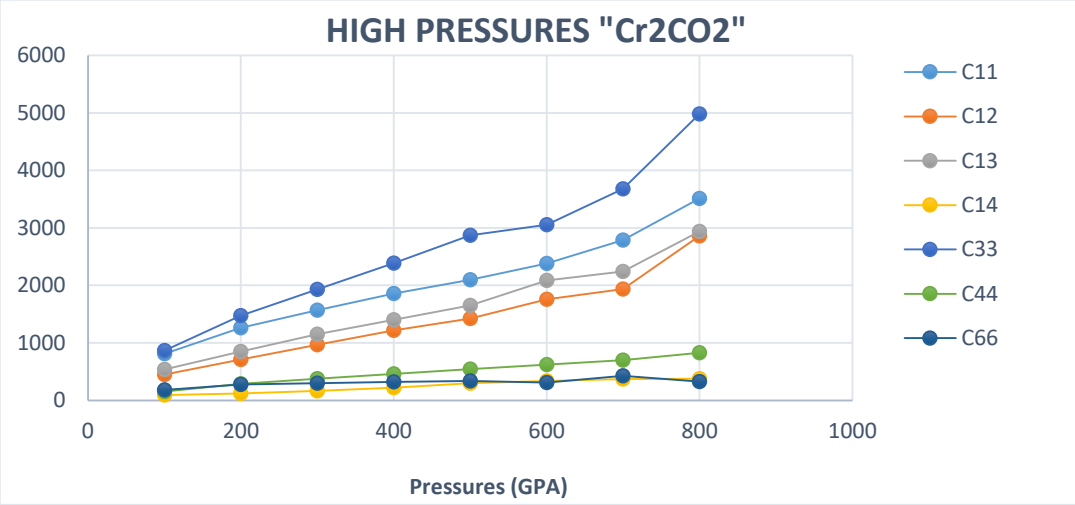
(e)


C44
Cr2CO2
Série2
Série3
Elasticity tensor C33
Pressures (GPA)

(f)



(g)



(h)

Figure IV-15: (a), (b), (c), (d), (e), (f), (g): variations of the 7 elasticity tensors as a function of pressure for the three MXenes, **(h):** high pressure of Cr_2CO_2 for the 7 elasticity tensors.

IV.4.4 Effect of pressure variation on the elastic properties of Cr_2CO_2 and $Cr_2C(OH)_2$:

The CASTEP code computes stress tensors and various elastic properties of the Cr_2CO_2 and $Cr_2C(OH)_2$ materials, including shear and Bulk Modulus (G, β) (see equations II.**3** and II.4), Poisson's ratio (ϑ) (see equation II.6), Young's modulus (E) (see equationII.5), utilizing the Hill approximation for calculation at different pressures.

The values gathered from these properties calculated by CASTEP for the both structures are displayed in the (Table IV-7 and Table IV-8).

- **Cr_2CO_2 MXene:**

Table IV-7: Elastic properties behavior during compression (Cr_2CO_2).

Pressure (GPA) / ***Properties***	β (GPA)	G (GPA)	ϑ (GPA)	E (GPA)
0	32.80089	-47.4271	1.89558	-274.658
10	142.822	33.74767	0.39048	93.85093
20	270.3775	62.54228	0.39262	174.1955
30	329.362	70.09296	0.40064	196.3502
40	371.0563	86.51581	0.39183	240.8301
50	389.6756	86.57119	0.39658	241.8068
60	435.8905	71.81929	0.42191	204.2407
80	513.7376	94.50243	0.41334	267.1278
100	610.4991	139.7462	0.39366	389.5177
200	969.6104	253.8803	0.37959	700.5017
300	1.27E+03	293.9031	0.39257	818.563
400	1.54E+03	330.7654	0.40008	926.1967
500	1.79429E+03	337.82441	0.41142	953.62444
600	2.13E+03	314.62709	0.4295	9.00E+02
700	2.41E+03	433.61283	0.41497	1.23E+03
800	3.22E+03	4.35E+02	0.4353	1.25E+03

From the Table IV-7 we see that the Poisson's ratio is higher than 0.33 indicates that Cr_2CO_2 exhibits a very high lateral deformation to axial deformation.

➢ $Cr_2C(OH)_2$ MXene:

Table IV-8: Elastic properties behavior during compression ($Cr_2C(OH)_2$).

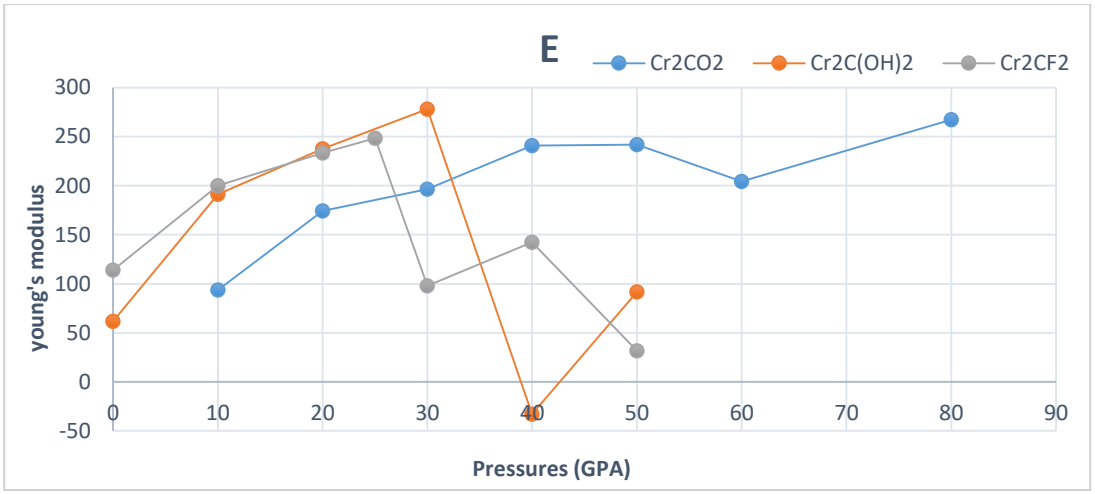
Pressure (GPA) / ***properties***	β (GPA)	G (GPA)	ϑ (GPA)	E (GPA)
0	22.47455	29.50933	0.04335	61.57738
10	180.80802	72.20984	0.32377	191.17895
20	239.74190	88.95432	0.33490	237.49004
30	276.79574	104.36694	0.33252	278.14256
40	342.35054	-10.87718	0.51606	-32.98082
50	386.82535	31.35456	0.46054	91.58906

From the Table IV-7 and Table IV-8 we notice that the Bulk Modulus (β) is higher compared to the Shear Modulus (G), which indicates that the material is more resistant to change in volume (compression) than to change in shape (Shear).

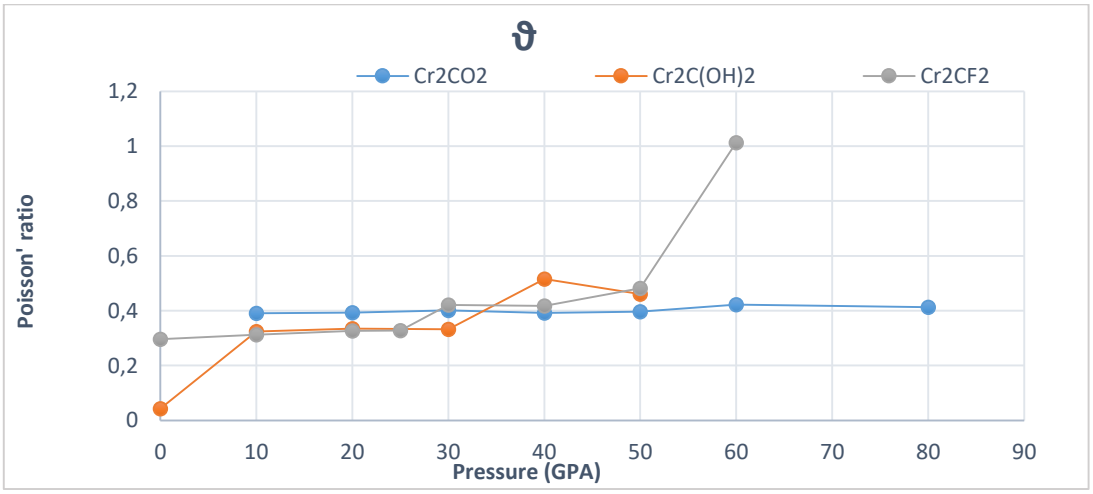
We also note that the young's modulus increases linearly with changing pressure and these values are relatively important, the greater its value, the more difficult the material is to deform uniaxially.

Concerning the variation of the Poisson's ratio of $Cr_2C(OH)_2$ (see Table IV-8) which measures the stability of the crystal against shear, it increases as a function of pressure and as the values are less than 0.33 (limit of metallic materials) and greater than 0.1 (limit of covalent materials), we can conclude the existence of mixture between covalent, ionic and metallic bonds from the region [10 to 30 GPA].

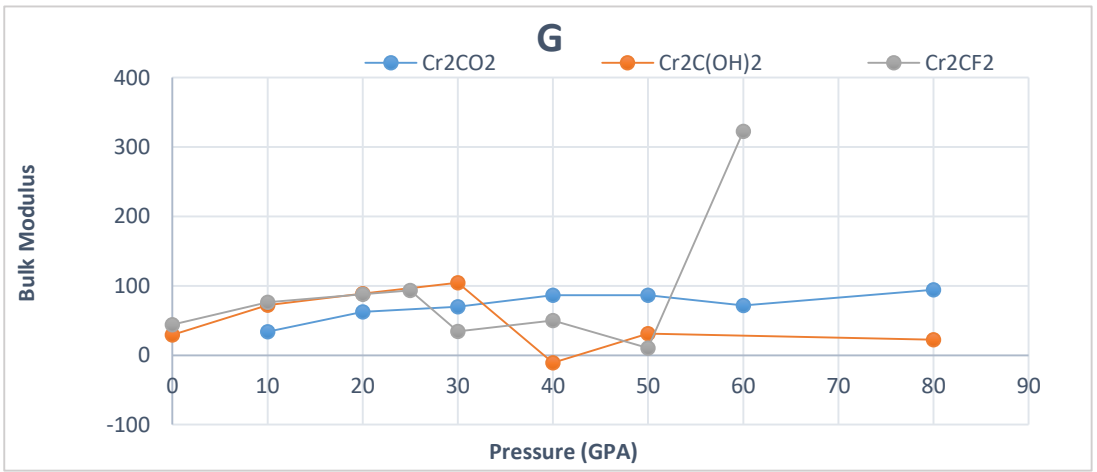
To elucidate the evolution of these properties we have plotted them in Figure IV-16.



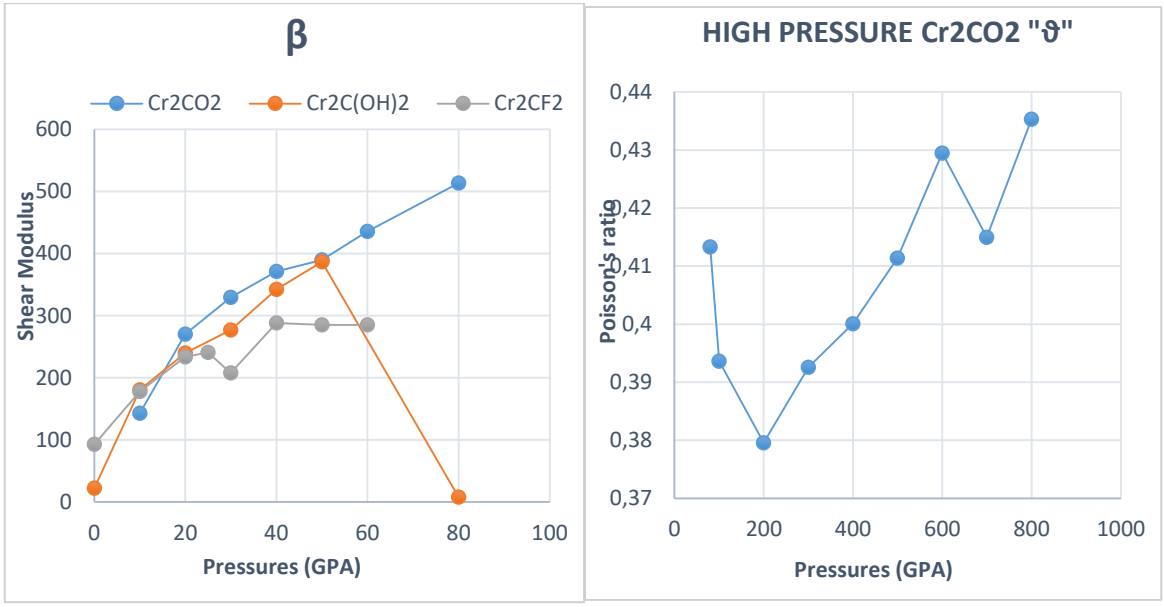
(a)



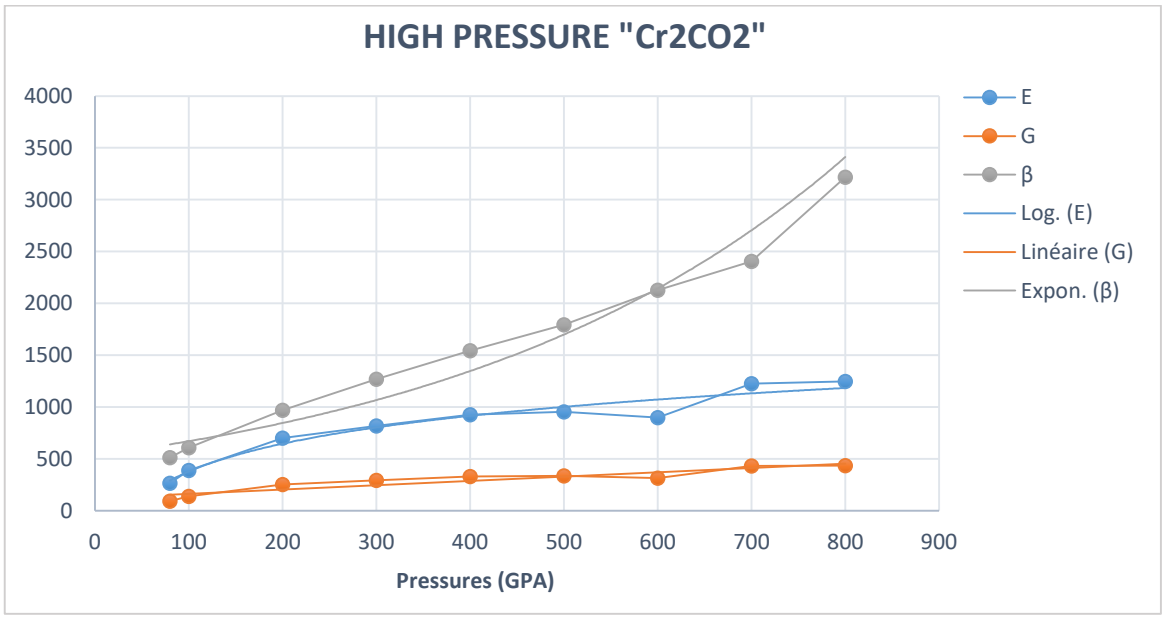
(b)



(c)



(d) **(e)**



(f)

Figure IV-16: (a), (b), (c), (d): variations of the elastic properties as a function of pressure for the three MXenes, **(e), (f):** high pressure of Cr_2CO_2 for different elastic properties.

IV.4.5 Study of the ductility of Cr_2CO_2 and $Cr_2C(OH)_2$ structures:

We calculate and determined the G/β ratio for the Cr_2CO_2 and $Cr_2C(OH)_2$ Materials, which shows MXene's ductility, and the results are shown in (Table IV-9) for further illustration, we have reported the behavior in Figure IV-17 which shows the fluctuation of the Pugh ratio K= G/β as a function of pressure.

Table IV-9: values of the ductility ratio and Cauchy pressure.

	G/β		$C''=C_{12}-C_{44}$	
Pressure GPa	Cr_2CO_2	$Cr_2C(OH)_2$	Cr_2CO_2	$Cr_2C(OH)_2$
10	0.2362919	0.399373	144.1654	160.6082
20	0.2313147	0.371042	188.1568	178.3547
30	0.2128144	0.377054	207.5121	187.288
40	0.2331609		188.7334	223.3502
50	0.2221622		198.3351	233.9809

The Pugh ratio β/G provides insight into the mechanical properties of the materials under various pressures.

Metals with a high G/β ratio were typically brittle, but those with a low G/β ratio were typically ductile. The transition from ductile to brittle behavior was not identified by Pugh, but subsequent investigation of other crystalline alloy systems revealed that brittle behavior would be typical when G/β ≥0.57-0.6. Pettifor's criterion states that material with non-directional metallic bonds is intrinsically ductile and has positive Cauchy pressure (C" >0), while material with negative Cauchy pressure (C"<0) is directional and brittle, whereas C"=C_{12}-C_{44} [52].

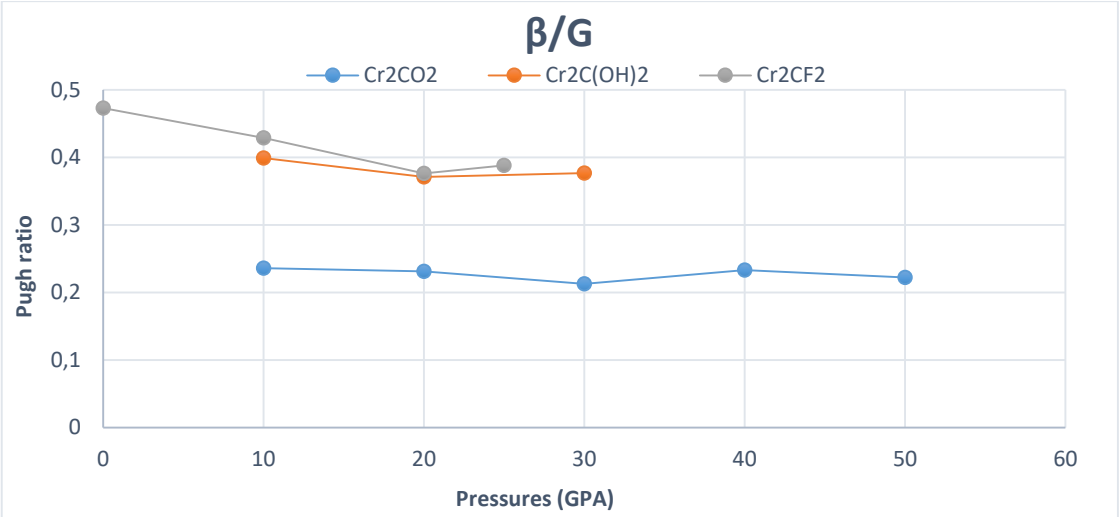
The Table IV-9 provide the values of K=G/β (shear to bulk modulus), which shows us that:

- ✓ **Cr_2CO_2:**

The G/β ratio remains consistently around 0.2 across the pressure range from 10 to 50 GPA. Since the ratio is well below the critical value of 0.57 to 0.61, Cr_2CO_2 can be considered highly ductile across the entire pressure range. In addition, the values of C" remain positive, so according to Pettifor's criterion Cr_2CO_2 possesses non-directional metallic bonds and is intrinsically ductile at all pressures considered.

- ✓ **$Cr_2C(OH)_2$:**

At pressure from 10 to 30 GPA, the G/β ratio decreases significantly, well around 0.3, which indicates ductility. In addition, the value of C" are positive across all pressures, indicating that $Cr_2C(OH)_2$ possesses non-directional metallic bonds and is intrinsically ductile.



(a)

Figure IV-17: (a): representation of the G/β ratio for the three MXenes.

IV.4.6 Chen and Tian hardness:

$H_{V,Chen}$ and $H_{v,Tian}$ represent the estimated Vickers hardness according to the Chen (equation IV.1) and Tian (equation IV.2) formulas, respectively. K is the Pugh ratio, G typically represents the shear modulus [53].

$$H_{V,Chen}=2(K^2\mathrm{G})^{0.585}-3 \qquad \textbf{IV.3}$$

$$H_{V,Tian}=0.92K^{1.137}G^{0.708} \qquad \textbf{IV.4}$$

The Chen and Tian values obtained for the two materials, Cr_2CO_2 and $Cr_2C(OH)_2$, are shown in Table IV-10. To understand the changes more, we represent them in Figure IV-18.

Table IV-10: values of Pugh ratio, shear modulus, Chen and Tian hardness for both materials.

	Cr_2CO_2				$Cr_2C(OH)_2$			
	K	**G**	**H_{Tian}**	**H_{Chen}**	**K**	**G**	**H_{Tian}**	**H_{Chen}**
10	0.236292	33.74767	2.1547444	-0.102738	0.399373	72.20984	6.7056618	5.35452878
20	0.231315	62.54228	3.2552016	1.0542395	0.371042	88.95432	7.1487832	5.65999639
30	0.212814	70.09296	3.2096853	0.9310693	0.377054	104.36694	8.1526958	6.68905626
40	0.233161	86.51581	4.1331007	1.9475256				
50	0.222162	86.57119	3.913922	1.6773247				

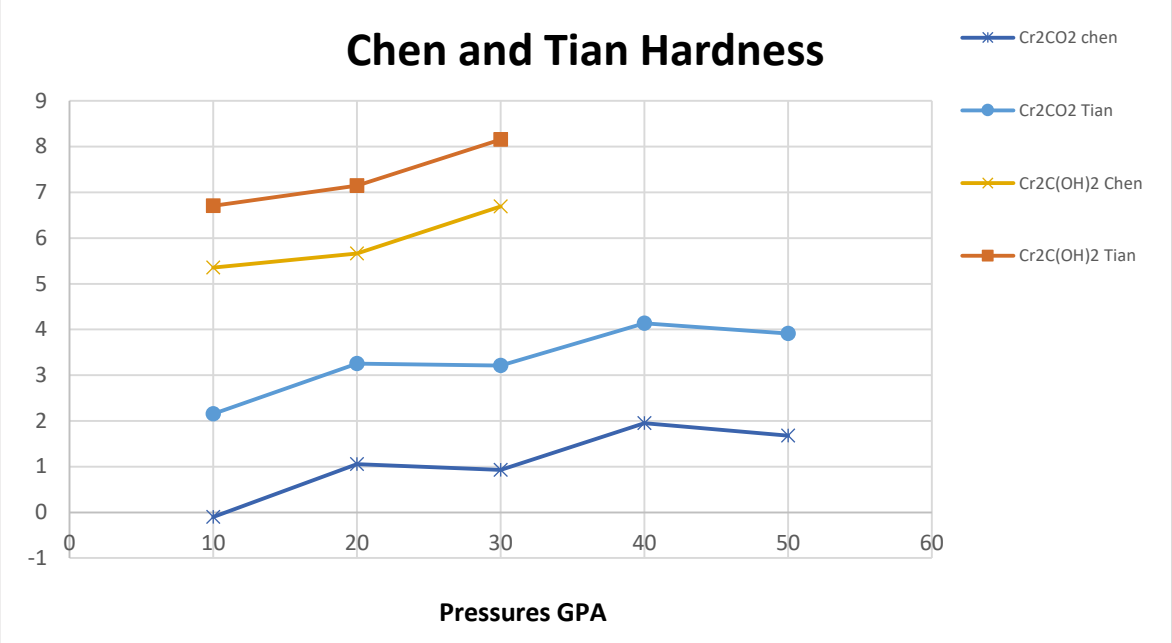


Figure IV-18: Chen and Tian hardness for both Cr_2CO_2 and $Cr_2C(OH)_2$ MXenes.

Through the Table IV-10 and Figure IV-18 obtained, we notice and conclude that:

✓ Cr_2CO_2:

The hardness values (both Chen and Tian) are relatively low, starting from negative or small values at lower pressures and increasing modestly with pressure. This indicate that Cr_2CO_2 is a softer material with lower hardness values and more fluctuation with pressure changes.

✓ $Cr_2CO(OH)_2$:

Shows significantly higher hardness values compared to Cr_2CO_2, and the values increase consistently with pressure. This indicates that $Cr_2CO(OH)_2$ is a harder material and less sensitive to pressure change compared to Cr_2CO_2.

✓ Comparison of Cr_2CO_2 and $Cr_2CO(OH)_2$ with Diamond and Steel:

- As well known that Diamond is the hardest natural material, has a Vickers hardness (Hv) of about ~70 GPA (7000 kgf/mm^2), which is significantly higher than both Cr_2CO_2 and $Cr_2CO(OH)_2$.
- The hardness of steel varies widely depending on the alloy and treatment, but typical values for hardened steel rang from ~2 to 9 GPA (200 to 900 kgf/mm^2), which is significantly softer than $Cr_2CO(OH)_2$ but comparable to or harder than Cr_2CO_2.

IV.5 GENERAL CONCLUSION:

In this work, we have investigated how compression affected the structural and elastic properties of the Cr_2CO_2 and $Cr_2CO(OH)_2$ MXenes materials. Since they are extremely important to science and technology. Density functional theory (DFT)-based ab-initio computation techniques were employed. Important information on anisotropy, interatomic bonding, and structural stability is conveyed by the values of elastic constants and lattice parameters.

As a result of the structure, it was discovered that MXene's crystal structure is influenced by the terminal OH and O groups. A decrease in lattice parameters under pressure indicates that the edges of the unit cell are being compressed, bringing the atoms closer together, and as the lattice parameters decrease, the overall volume of the unit cell also reduces, indicating a more compact structure.

Moreover, we calculate by the ab-initio approach the elastic properties of both Cr_2CO_2 and $Cr_2C(OH)_2$ MXenes described by the seven independent stiffness constant C_{11}, C_{12}, C_{13}, C_{14}, C_{33}, C_{44}, and C_{66}. The values of C_{11} and C_{33} always rises as the pressure rises in both materials indicates that the material becomes stiffer and more resistant de deformation along the a-axis and c-axis. On the other hand, there is an increase in the values of C_{12} and C_{13} for Cr_2CO_2 also, indicates that the material becomes more resistant to shear deformations and inter-plane stresses.

Cr_2CO_2 and $Cr_2C(OH)_2$ exhibit distinct elastic behaviors and hardness characteristics under varying pressures. The analysis reveals that Cr_2CO_2 and $Cr_2C(OH)_2$ material are ductile from their pressure range, based on their G/β ratio through the critical threshold for ductility. Additionally, the positive (C") values for both materials indicate non-directional metallic bonds. According to Pettidor's criterion, this confirms that $Cr_2C(OH)_2$ and Cr_2CO_2 possess non-directional metallic bonds and are intrinsically ductile at all pressures considered. Moreover, $Cr_2C(OH)_2$ exhibits higher hardness than most Steels, making it suitable for applications demanding greater wear resistance, but it is still significantly softer than Diamond, while Cr_2CO_2 has lower hardness values, making it less suitable for high-hardness applications compared to steel, $Cr_2C(OH)_2$, and Diamond.

In this work, we have also assembled our obtained results in with the results of last year to see well how Cr_2C MXene was affected by the terminations F, OH, and O. and we conclude that Cr_2CO_2 appears to have the highest and most stable increase in stiffness under pressure,

making it potentially more reliable in high-pressure environments compared to $Cr_2C(OH)_2$ and Cr_2CF_2.

Finally, we can say that this study demonstrates that termination groups play a crucial role in modulating the mechanical and structural properties of Cr_2C MXene, providing a pathway to engineer for advanced technological applications.

BIBLIOGRAPHIC REFERENCE

[1] Olha Mashtalir, "Chemistry of Two-Dimensional Transition Metal Carbides (MXenes)," pp. 1-175, June 2015.

[2] L. J, L. L, L. K.H, . B. Shahid, R. K and R. S, "How viable are MXenes? Recent developments of MXene synthesis and its application in solid-state electrolytes," *Energy Storage,* vol. 84, p. 110868, 2024.

[3] G. Yury and . H. Qing, "MXenes: Two-Dimensional Building Blocks for Future Materials and Devices," *ACS NANO,* p. 5775–5780, 27 APRIL 2021.

[4] . T. Mengrao, . L. Jiaming , W. Yu , H. Wenjuan, X. Shichong, L. Ming, . Z. Wei and L. Haibo, "Surface Terminations of MXene: Synthesis, Characterization, and Properties," pp. 1-42, 24 OCTOBER 2022.

[5] S. Maxim, N. Varun, K. Sankalp and W. B. Michel, "On the Chemical Diversity of the MAX phases," *trends in chemistry,* vol. 1, pp. 210-223, may 2019.

[6] . H. Joseph, "Synthesis and transport properties of 2D transition metal carbides (MXenes)," 2018, pp. 1-82.

[7] . K. Niels, B. Carina, S. Jordan , M. S. Rose and S. B. Christina , "Extending the Chemistry of Layered Solids and Nanosheets:Chemistry and Structure of MAX Phases, MAB Phases and MXenes," *ChemPlusChem,* pp. 1-23, 2023.

[8] D. Martin, R. Johanna and A. Björn, "Stability trends of MAX phases from first principles," *The American Physical Society,* pp. 220102(1)-220102(4), 23 June 2010.

[9] V. Gray, "Ti3SiC2 and Ti3Al2 single crystal Elastic Shear Modulus: Investigation via Inelastic Neutron Scattering and Computer Simulation," *ResearchGate,* May 2014.

[10] . E. Per, . B. Manfred, J. Ulf , . H. Hans and . H. Lars, "The Mn+1AXn phases: Materials science and thin-film processing," pp. 1-113, 2010.

[11] G. J. Jesus, "Processing of MAX phases: From synthesis to applications," *American ceramic society ,* pp. 659-690, 30 September 2020.

[12] . M. Sayed, . D. Walid, I. Ahmed and N. Erich, "Hot Forging and Hot Pressing of AlSi Powder Compared to Conventional Powder Metallurgy route," *Materials Sciences and Application,* pp. 1127-1133, 12 june 2011.

[13] . A. N.N, . D. S.K, . T.-G. O.P, . M. G.N and H. A.A, "Self-propagating high-temperature synthesis of MAX phases in Ti–Zr–Al–C system (C:P15)," *Ceramics International,* vol. 49, pp. 24165-24170, 15 July 2023.

[14] . B. Abhijit, . N. Varun and P. Anand B, "Thin-film growth of MAX phases as functional materials," *Materials Science,* vol. 1, pp. 1-11, 24 decembre 2021.

[15] . R. H. Dumooa, . K. A. Khalid and . M. . A. A.-G. Ahmed, "Overview of structural, electronic, elastic, thermal, optical, and nuclear properties of Zr2AC (A= Al, Si, P, S, Ge, As, Se In, Sn, Tl, and Pb) MAX phases: A brief review," *Heliyon,* vol. 9, pp. 1-31, 13 July 2023.

[16] N. Michael , W. B. Michel and . G. Yury, "Ten Years of Progress in the Synthesis and Development of MXenes," pp. 1-27.

[17] . C. Aur´elie and C. C. Jean, "Physical properties of 2D MXenes: from a theoretical perspective," *Journal of Physics: Materials,* pp. 1-22, 26 October 2020.

[18] . G. Yury and A. Babak , "The Rise of MXenes," *ACS NANO,* pp. 8491-8494, 27 august 2019.

[19] . R. Kang, . L. Garrick, S. Mikhail , C. W. Brian, A. Babak , . G. Yury and W. S. Zhi , "Fundamentals of MXene synthesis," *nature synthesis,* vol. 1, pp. 601-614, 1 AUGUST 2022.

[20] L. Guohao , L. Shuhan , w. jie, . X. Guanshun, . Z. Nan and X. Xiuqiang, "Surface chemistry engineering and the applications of MXenes," *Materiomics,* vol. 9, pp. 1160-1184, 2023.

[21] . D. Duraisami, A. E.-h. Mamdouh, R. B, b. Abdullah and A. Fathre, "MXenes: A promising material with multifunctional applications," *Environmental Chemical Engineering,* vol. 12, pp. 1-17, 22 FEBRUARY 2024.

[22] . V. Louisiane, . N. Varun, . C. Michael and W. B. Miche, MXenes: An Introduction of their Synthesis, Select Properties, and Applications, Materials Science and Engineering, 2019, p. 11.

[23] R. r. M. deepthi jayan k, "Electronic, electrical and optical properties of MXenes," in *MXene Reinforced Polymer Composites*, 2024, pp. 107-145.

[24] M. H. ,. G. ,. U. ,. U. K. ,. M. E.-M. K. Ubaid Ur Rahman, "MXenes as Emerging Materials: Synthesis, properties and applications," *Molecules,* vol. 27, pp. 1-36, 2022.

[25] . H. Jing, L. Zhe, M. Yukun and L. Zhou , "Progress and biomedical applications of MXenes," *nano select WILEY,* pp. 1480-1508, 2021.

[26] R. G. M. B. L. Z. Q. ,. G. H. L. b. Z. L. ,. H. R. Jinbo Pang, "Applications of 2D MXenes in energy conversion and storage systems," *Royal society of CHEMISTRY,* vol. 48, pp. 72-133, 7 January 2019.

[27] "https://www.chm.bris.ac.uk/webprojects2003/cook/latticetypes.htm," [Online].

[28] P. P. S. P. D. Rostam Golesorkhtabar, "ElaStic: A universal tool for calculating elastic constants from first principles," *RsearchGate,* pp. 1-20, March 2015.

[29] A. R. a. B. A. Brian C. Wyatt, "2D MXenes: Tunable Mechanical and Tribological Properties," *ADVANCED MATERIALS PERSPECTIVE,* vol. 33, pp. 1-20, 28 April 2021.

[30] S. M. Subramanian, "Mechanical properties of materials: Definition, testing and application.," *International journal of modern studies in mechanical engineering,* vol. 6, pp. 28-38, 2020.

[31] ,. N.-H. H. ,. H. T. D. ,. M. P. T. T. T. Ngoc Lan Mai, "Elastic and thermodynamic properties of the major clinker phases of Portland cement: Insights from first principles calculations.," *Construction and Building Materials,* vol. 287, p. 122873, 2021.

[32] P. Anne Marie Helmenstine, "What Is Young's Modulus?," 12 Novembre 2019. [Online].

[33] "SCIENCE NOTES," [Online].

[34] A. M. ,. M. A. ,. E. M. A. E. Yassmin Ibrahim, "The Recent Advances in the Mechanical Properties ofSelf-Standing Two-Dimensional MXene-Based Nanostructures: Deep Insights into the Supercapacitor," *Nanomaterials,* vol. 10, p. 1916, 2 Septembre 2020.

[35] R. P. ,. Y. Y. H. ,. W. ,. L. S. Xianshi Zeng, "Pressure Effect on Elastic Constants and Related Properties of Ti3Al Intermetallic Compound:A First-Principles Study.," *Materials,* vol. 11, pp. 1-16, 2018.

[36] M. Félix, "Necessary and Sufficient Elastic Stability Conditions in Various Crystal Systems," *ResearcgGate,* vol. 90, pp. 1-4, 2014.

[37] A. V. K. B. G. Å. Z. N. P. Xiantao Jiang, "Two-dimensional MXenes: From morphological to optical,electric, and magnetic properties and applications," *Physics Reports,* vol. 848, pp. 1-58, 15 March 2020.

[38] Z. L. M. L. Jing Huang, "Progress and biomedical applications of MXenes," *Nano select WILEY,* p. 1480–1508, 2021.

[39] . A. Swarnima, A. . M.-B. Stefano, . A. Kailash, . K. Vrushali, L. L. Jodie , R. Miladin and J. G. Micah, "Effect of terminal groups on the degradation stability of Ti3C2Tz MXenes," *The Royal Society of Chemistry,* pp. 12567-12573, 11 July 2023.

[40] T. Su, X. MA, . J. Tong, . H. Ji, Z.-Z. Qin and Z. Wu, "Surface engineering of MXenes for energy and environmental applications," *Journal of Materials Chemistry A,* pp. 1-73, 31 mars 2022.

[41] . R. Komal and . K. Anish, "Handbook of Functionalized Nanostructured MXenes," in *Synthetic Strategies and Applications from Energy to Environment Sustainability*, 2023, pp. 1-387.

[42] B. Zhuoheng , L. Chengjie, C. Xin, Z. Peigen , Y. Li, . Z. Heng, S. Dawei, H. Wei, Z. Wei, P. Long and S. Zhengming, "Role of MXene surface terminations in electrochemical energy storage: A review," *Chinese Chemical Letters,* vol. 32, pp. 2648-2658, 6 February 2021.

[43] W. Yifan, X. Yanheng, H. Menglei, L. Han and Z. Xi, "MXenes: focus on optical and electronic properties and corresponding applications," *Nanophotonic,* vol. 9, p. 1601–1620, 2 April 2020.

[44] Z. Lin , . S. Weiwei, . L. Hongshi, D. Hong, Y. Yibo and C. Ruihan, "Influencing Factors on Synthesis and Properties of MXene: A Review," pp. 1-13, 1 Septembre 2022.

[45] . M. Mohammad and . S. Masoud, "Surface functionalization of MXenes," pp. 7277-7307, 20 SEPTEMBRE 2021.

[46] K. L. Q. L. Q. H. J. H. X. W. a. S. D. Xian-Hu Zha, "Role of the surface effect on the structural, electronic," *IOP SCIENCE,* pp. 26007-p1-26007-p6, 20 july 2015.

[47] "Dassault Systèmes," [Online].

[48] *BIOVIA Materials Studio version 20.1.0.2728,* 2020.

[49] T. L. W.-G. H. T. R. T. F. H. L. Noodleman, "Density Functional theory," *Chemistry II,* vol. 2, pp. 491-510, 2003.

[50] J. Z. S. Chen Si, "Half-metallic ferromagnetism and surface functionalization-induced metal-insulator transition in graphene-like two-dimensional Cr2C crystals," *ACS Applied Materials & Interfaces,* pp. 1-17.

[51] B. R. Z. N. Krea Mohamed, Etude de l’effet des groupements terminaux Tx sur les propriétés structurales et mécaniques d’un MXène Cr2C: cas du Fluor, Département du génie des procèdes et de, 2022/2023, pp. 1-96.

[52] O. N. S. &. D. B. Miracle, "Generalization of intrinsic ductile-to-brittle criteria by Pugh and Pettifor for materials with a cubic crystal structure," *Scientific reports*, pp. 1-4, 2021.

[53] M. O. T. H. M. Al-Fahdi, "High-Throughput Computation of Novel Ternary B-C-N Structures and Carbon Allotropes with Electronic-Level Insight into Superhard Materials from Machine Learning," *Materials Chemistry A*, pp. 1-28, 29 Oct 2021.